Palaeogeography, Palaeoclimatology, Palaeoecology 636 (2024) 111970

Contents lists available at ScienceDirect

Palaeogeography, Palaeoclimatology, Palaeoecology

journal homepage: www.elsevier.com/locate/palaeo

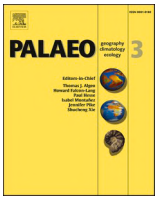

Stress precursors of the Messinian salinity crisis as recorded by calcareous plankton and geochemistry in the Eastern Mediterranean: The Upper Metochia section of the Gavdos Island (Greece)

Rocco Gennari [a,b,*], Stefano Lugli [c], Vinicio Manzi [b], Davide Persico [b], Matteo Reghizzi [b], Marco Roveri [b]

[a] Department of Earth Sciences, University of Torino, Via Valperga Caluso, 35, 10125 Torino, Italy
[b] Department of Chemistry, Life Sciences and Environmental Sustainability, University of Parma, Via delle Scienze, 157/A, 43124 Parma, Italy
[c] Department of Chemistry and Geological Sciences, University of Modena and Reggio Emilia, via Giuseppe Campi, 103, 41125 Modena, Italy

ARTICLE INFO

Editor: H Falcon-Lang

Keywords:
$^{87}Sr/^{86}Sr$
Foraminifera
Calcareous nannofossil
$\delta^{18}O$ and $\delta^{13}C$
Marine environmental stress
Restricted circulation

ABSTRACT

The road to the Messinian salinity crisis was paved with increasing environmental stress in the Mediterranean marine realm. The nature and origin of the crisis of the marine biota is still matter of debate because the crisis itself hinders univocal paleoenvironmental reconstructions by selecting the most resilient taxa, which are generally adapted to a wide range of stresses. The commonly accepted hypothesis, recently reiterated, is that increasing salinity was the main factor eliminating the marine biota from the geological record and eventually leading to the deposition of evaporitic carbonates in the Eastern Mediterranean just before the onset of the crisis dated at 5.97 Ma. We suggest that stratification and increasing restriction (continental water influence), leading to strong variability of surface water conditions, better explain the $^{87}Sr/^{86}Sr$ excursion below the global ocean value and the pattern of calcareous plankton events in the uppermost portion of the Metochia section (Gavdos Island, Greece), from 6.24 to 5.95 Ma. The early reduction of foraminifera at 6.07 Ma, typical of relatively deep successions lacking primary gypsum during the first phase of the crisis, precedes a sequence of calcareous nannofossil events such as the influx of *Braarudosphaera bigelowi* at 6.168 Ma, the acme of *Reticulofenestra perplexa* at 6.058–6.018 Ma, and the peaks of *Sphenolitus* spp. and *Helicosphaera carteri* at 5.99 and 5.973 Ma, respectively. The peak of such opportunistic calcareous nannofossil and the foraminifer disappearance, commonly observed in both deep and shelf successions, closely approximate the onset of the Messinian salinity crisis, regardless the occurrence of the Primary Lower Gypsum unit, and is interpreted as the final restriction step, which led to a 600 ky environmental perturbation culminating with the deposition of the Mediterranean salt giant.

1. Introduction

The paleoenvironmental events associated to the uppermost pre-evaporitic cycles before the onset of the Messinian salinity crisis (MSC; 5.97 Ma; Manzi et al., 2013) have recently lead to the reconstruction of two alternative scenarios: 1) the increase of restriction and continental influence (Sorbas Basin, Western Mediterranean; Mancini et al., 2020) and 2) the early onset of evaporitic conditions (at around 6 Ma), marked by limestone deposition in the Gavdos Island, Eastern Mediterranean, and in the Falconara section of Sicily, Central Mediterranean (Zachariasse and Lourens, 2021). These two different scenarios are both reached after a long progression starting from 7.16 Ma and punctuated by paleoceanographic steps at 6.7, 6.4 and 6.1 Ma (Kouwenhoven et al., 2006; Roveri et al., 2014a; Corbí et al., 2020), depicting an oceanographic perturbation with common characteristics in all the Mediterranean. The hydrological progression finds its most obvious origin in the tectonic restriction of the Atlantic connections in the Betic and Rifian regions (Duggen et al., 2003; Garcia-Castellanos and Villaseñor, 2011; Hüsing et al., 2012; Capella et al., 2018, 2019), which slowed the thermohaline circulation and increased the sensitivity of the Mediterranean to orbital driven climatic changes. Superimposed Late Miocene high and low latitude climatic events are the onset of Northern

* Corresponding author at: Department of Earth Sciences, University of Torino, Via Valperga Caluso, 35, 10125 Torino, Italy.
E-mail address: rocco.gennari@unito.it (R. Gennari).

https://doi.org/10.1016/j.palaeo.2023.111970
Received 17 July 2023; Received in revised form 23 November 2023; Accepted 11 December 2023
Available online 14 December 2023

Hemisphere glaciations and intensification of the Asian and African Monsoon (Holbourn et al., 2018).

Since 7.16 Ma the preservation of organic matter on the deep Mediterranean sea-floor is enhanced and sapropelitic marls (referred to herein sapropels) start to form regularly at precession minima (insolation maxima) in deep to intermediate settings such as those of the Monte del Casino, Falconara and Metochia sections (Hilgen and Krijgsman, 1999; Krijgsman et al., 2004). Sapropels are commonly overlain by diatom rich hemipelagic sediments (e.g., the Tripoli Formation of Sicily), which diachronously appear from 7.16 to 6.7 Ma, in turn followed by homogeneous marls deposited at increasing precession phases (e.g., Blanc-Valleron et al., 2002). Microfossils recorded this perturbation with the disappearance of oxyphilic benthic foraminifera from the sea floor at 7.16 Ma (Kouwenhoven et al., 2006) and, from 6.7 Ma, with the alternating dominance in surface waters of calcareous plankton taxa adapted to warm/oligotrophic and cold/eutrophic conditions during insolation maxima and minima, respectively (Sierro et al., 2003). From 6.4 Ma, the same periodicity is recorded by alternating low and high planktic/benthic (P/B) foraminifer ratio (Sierro et al., 2003; Gennari et al., 2018). The periodicities observed from 6.7 and 6.4 Ma are related to enhanced river runoff and precipitation during insolation maxima, that triggered stratification of the water column and sea floor de-oxygenation, and drier and cooler climate during insolation minima, favoring mixing and nutrient injection in surface waters (Bellanca et al., 2001; Sierro et al., 2003; Gennari et al., 2018; Mancini et al., 2020). Such a strong imprint of orbital parameters on the biota and the sedimentation allowed the reconstruction of a high-resolution integrated stratigraphic framework based on biostratigraphic and magnetostratigraphic events and radiometric age constrain (Krijgsman et al., 1999; Krijgsman et al., 2004; Manzi et al., 2013; Tzevahirtzian et al., 2023). The framework is characterized by a bed-by-bed correlation across the Mediterranean, documenting the overall synchronous paleoceanographic evolution from west to east.

The suggested different scenarios at the MSC onset according to the interpretation of Zachariasse and Lourens (2021) are apparently supported by more stressed pre-evaporitic conditions of the Eastern Mediterranean as recorded on the Cyprus Island (Kouwenhoven et al., 2006; Gennari et al., 2018) in respect to the Western sector.

Moreover, Zachariasse and Lourens (2021) also suggest that in the Metochia (Gavdos) and Falconara (Sicily) sections the MSC onset is marked by a supposedly evaporitic limestone deposited at 6 Ma; thus, predating the age of the very first gypsum bed of the Primary Lower Gypsum unit (PLG unit of stage 1 of Roveri et al., 2008) of the Western and Northern Mediterranean, which is astronomically dated at 5.97 Ma (Manzi et al., 2013). Opposite to an earlier MSC onset, it is worth noting that a delayed gypsum deposition has been locally recognized in several basins, where the gypsum beds of the PLG unit pass downbasin to limestones, intercalated in an organic-rich argillaceous unit deposited in deeper and less oxygenated conditions (Manzi et al., 2007, 2011, 2018, 2021; Gennari et al., 2013; Dela Pierre et al., 2011; Roveri et al., 2020). Further moving towards deeper settings, both gypsum and limestone disappear and only organic-rich shale deposits are found, characterized by the absence of foraminifera and by the presence of opportunistic nannofossils associations (Lozar and Negri, 2019; Manzi et al., 2018). This variability implies the need of an integrated approach (e.g., micropaleontology, organic and inorganic geochemistry, magnetostratigraphy and cyclostratigraphy) in the recognition of the MSC onset in successions totally or partially free of gypsum beds (Manzi et al., 2021). As an example, Manzi et al. (2018, 2021) defined the foraminifer barren interval (FBI) as an evaporite-free shale unit recording the first stage of the salinity crisis in deep water settings equating the Non Distinctive Zone (NDZ of Lirer et al., 2019) in the Mediterranean planktic foraminifer biozonation. These observations led to remarkable stratigraphic implications: while the onset of the MSC occurred synchronously in the Mediterranean, the onset of the evaporite deposition was instead diachronous; thus, the base of the evaporites coincides with the crisis onset only locally. Moreover, the age of the evaporites seems not to be older than 5.97 Ma (Roveri et al., 2014a, 2014b).

In the frame of the debate concerning the timing and modality of the MSC onset we propose a new set of data from the Metochia section (Gavdos Island, south of Crete) (Fig. 1), one of the reference sections used to build the integrated chronostratigraphic framework (Krijgsman et al., 1999, 2004) and the reconstruction of the paleoceanographic evolution of the Mediterranean during the pre-evaporitic phase (Zachariasse and Lourens, 2021).

Our contribution is based on a precession-scale database composed of quantitative data on both calcareous nannofossils and foraminifera and $^{87}Sr/^{86}Sr$ isotopic stratigraphy. Moreover, we focus on the limestones close to the MSC onset including O and C stable isotope and petrography in order to detail their origin.

2. The Late Miocene of Gavdos: the Metochia section

The Late Miocene succession of the Gavdos Island (Fig. 1) was the object of several cyclostratigraphic, micropaleontological and paleoceanographic studies. Seidenkrantz et al. (2000) described the Tortonian - lower Messinian portion of the Metochia section (9.7 to 6.7 Ma) as a succession of cluster of three to four sapropels/marls couplets alternated with interval characterized by no or weakly developed sapropels, respectively corresponding to periods of eccentricity maxima and minima. From 7.16 Ma onward, they noted a more regular succession of sapropel/marl couplets, which turn into triplets from 6.7 Ma, when a diatomitic interval first occurs between the sapropel and marl (Hilgen et al., 1995; Zachariasse and Lourens, 2021). This is commonly documented in the Messinian pelagic sedimentary record of the Mediterranean (Blanc-Valleron et al., 2002; Kouwenhoven et al., 2003; Hüsing et al., 2009). Based on cyclostratigraphy and biostratigraphy (Hilgen et al., 1995) the sedimentary cycles of the Metochia section were tuned to the 65°N summer insolation curve, with sapropels mid-point corresponding to insolation maxima. Krijgsman et al. (2004) extended the tuning up to the first prominent limestone layer, which was considered an evaporitic deposit marking the onset of the MSC, at that time dated at 5.96 Ma (Fig. 2A). Zachariasse and Lourens (2021) recently revised the lithological log and cyclostratigraphy of the upper part of the section (Fig. 2A), redating the limestone bed at 6.00 Ma and confirming its evaporitic nature. The latter authors modified the lithological column of Krijgsman et al. (2004) as follows: 1) two cycles (M122 and M123) replace the thick diatomite layer containing the 1st influx of the left coiled *Neogloboquadrina acostaensis*; 2) the interval between the first and second limestone beds is now characterized by a thicker diatomite bed and by a thinner sapropel. This review led Zachariasse and Lourens (2021) to note a similarity with the Falconara section and to interpret the stratigraphic pattern as indicative of an earlier onset of the MSC in the Eastern and central Mediterranean respect to the Western and Northern Mediterranean as recorded in the Perales and Monticino sections (Manzi et al., 2013). Drinia et al. (2007) described a different lithological pattern for the Metochia section, with fewer diatomite beds (Fig. 2A) and a different upper part of the section, where the deposition of "medium grey limestones" coincides with the end of diatomite deposition; no sedimentological description was provided for these limestone beds.

3. Materials and methods

3.1. Petrographic analyses

The petrography of the sediments has been studied by optical microscopy under transmitted light using giant thin sections (45 × 60 mm). The thin sections were obtained using standard Logitech procedure from rock fragments impregnated in epoxy resin under vacuum. The thin sections have been stained for carbonate recognition using alyzarine red. XRD was performed to check the mineralogy of the samples and in

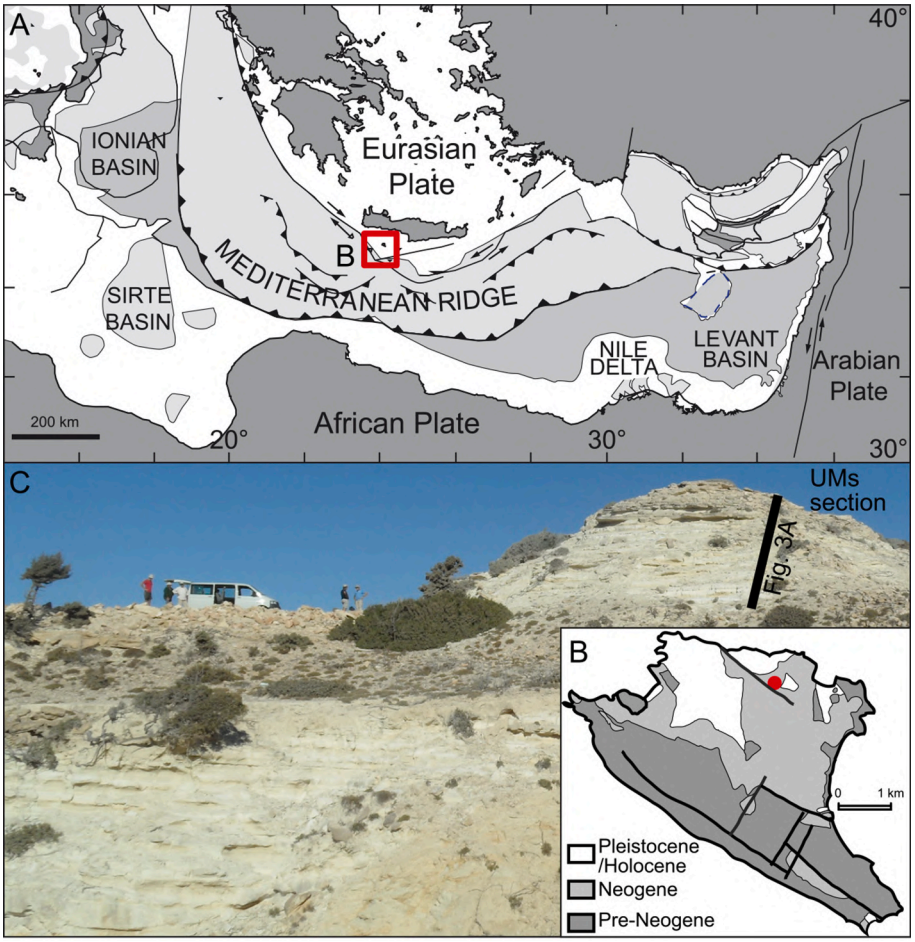

Fig. 1. Schematic geological map of the Eastern Mediterranean (A) and of the Gavdos Island (B, modified from Drinia et al., 2007), with the location of the Metochia section (black dot) and a panoramic picture of the outcrop (C). In C, the interval of the Metochia section studied in the present work is shown (UMs: upper Metochia section).

particular to assess the presence of dolomite in the carbonate layers.

3.2. Foraminifera

A total of 62 samples were first dried in an electric hoven at 40 °C, weighted and then soaked in diluted H_2O_2 for few days. Once the samples were disaggregated, they were washed with a 63 μm match sieve under tap water. The dried residues were then sieved again to obtain 63–125 and > 125 μm fractions. The latter was subdivided into aliquots to obtain ca. 300 planktic foraminifera, which were picked, classified, and stored in microslides. *Globigerinoides* and *Trilobatus* species (mainly *T. quadrilobatus* and *T. trilobus* and scarce *T. sacculifer*, *G. subquadratus*, *G. obliqus* and *G. extremus*) are lumped into the *Globigerinoides* group; the *Globigerinita* gr. is made up of prevalent *G. glutinata* and rare *G. uvula*; the few *Globigerina falconensis* observed in the samples are included in the *Globigerina bulloides* gr. The *Globoturborotalita* gr. includes *G. woodi*, *G. decoraperta*, *G. drury*, *G. nephentes* and *G. apertura*, all occurring in low percentages. The ratio between planktic and benthic foraminifera (P/B ratio) was calculated as P/(P + B)*100, where P and B are the number of planktic and benthic, respectively picked in the studied aliquots (the number of benthic foraminifera was often lower than 300). The abundance of planktic foraminifera was approximated by dividing the specimens counts in the aliquots by the weight (in gr.) of the corresponding dry sediment.

3.3. Calcareous nannofossil

Quantitative analysis of the calcareous nannofossil assemblages was carried out on standard smear-slides techniques (e.g., Bown and Young, 1998) from 61 samples, with a polarized light microscope at ×1250 magnification.

Species abundance was quantitatively evaluated: approximately 500 specimens were counted in defined number of fields of view (FOV) and, whereas in samples with a low total abundance, analyses were extended to more FOV. A proportion, into number of nannofossils per square millimeter, has subsequently standardized the data, collected in the primary range chart.

The taxonomic classification used the most recent traditional specific nomenclature. In some cases, like to small *Reticulofenestra* sp., the grouping corresponds to specimens not clearly classifiable with very small size (<5 μm). *Sphenolithus abies* has been counted since it represents a specie of palaeoecological value very useful for identifying the beginning of Messinian salinity crisis (MSC) (Manzi et al., 2007, 2018).

3.4. Strontium, oxygen and carbon isotope

Sr isotope analysis followed the methodology described in Reghizzi et al. (2017) and were performed at the CIGS (Centro Interdipartimentale Grandi Strumenti, University of Modena and Reggio Emilia). Planktic foraminifera and bulk samples were measured during two sessions when the NIST SRM 987 standard yielded a mean value of 0.71048 ± 0.000012 (2 S.D., $n = 22$) and 0.710250 ± 0.000008 (2 S.D.,

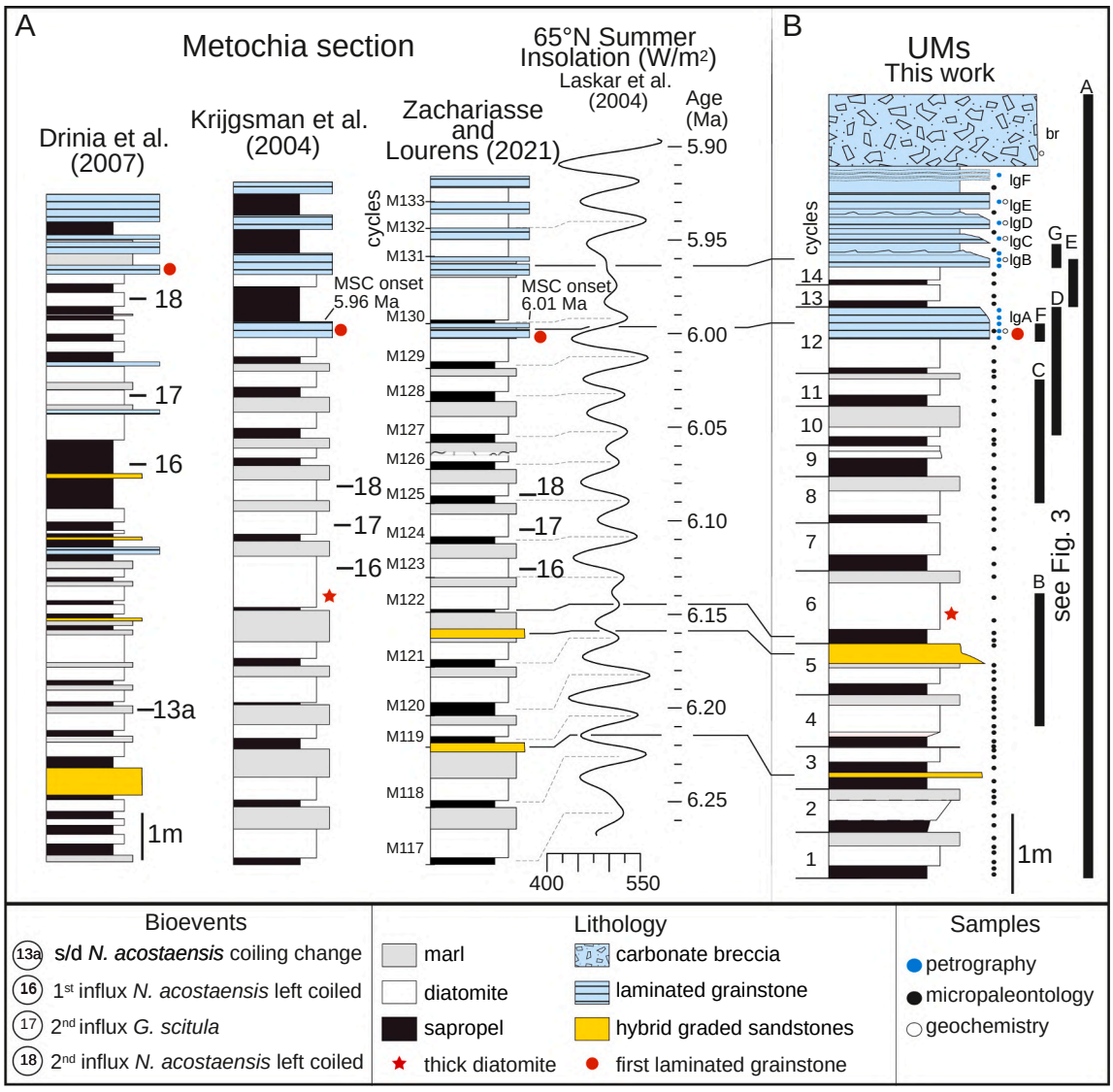

Fig. 2. Comparison of the lithological log of the Upper Metochia section (UMs) presented from previous works (A, Krijgsman et al., 2004; Drinia et al., 2007; Zachariasse and Lourens, 2021) and in this work (B). The astronomical tuning is illustrated for the log by Zachariasse and Lourens (2021). The key planktic foraminifer biostratigraphic events for the pre-MSC interval are numbered following Sierro et al. (2001), except 13a which indicates the coiling change from left to right of neogloboquadrinids. The age of the first prominent limestone bed (red circle) is indicated; in Krijgsman et al. (2004) and Zachariasse and Lourens (2021) this bed is interpreted as the MSC onset. A correlation based on the stratigraphic position of the thick diatomite (red star) and on the two hybrid graded sandstones is proposed among our log (B) and those of Krijgsman et al. (2004) and Zachariasse and Lourens (2021). To the right of our log, the position of the petrographic (blue dots), biostratigraphic (black dots) and geochemistry (white dots) samples are indicated; black vertical bars and letters correspond to the stratigraphic intervals shown in pictures of Fig. 3. (For interpretation of the references to colour in this figure legend, the reader is referred to the web version of this article.)

$n = 20$), respectively. For both analytical sessions, the internal precision on individual standard analysis varied between 0.000004 and 0.000008 (2σ) for all samples the instrument gave an average internal uncertainty value of 0.000010 (2σ), with a minimum value of 0.000005 and a maximum of 0.000018.

According to the oligotypic characteristic of planktic foraminifer assemblages and to the dominance of few species in the different lithology, a variety of species were used to obtain the $^{87}Sr/^{86}Sr$. However, where planktic foraminifera were scattered, absent or badly preserved, we also measured bulk samples in order to cover the section as much as possible. To test the reliability of bulk samples in respect to foraminifer shells, in several levels with different lithologies both materials were analysed.

Bulk samples were collected and measured for stable isotopes ($\delta^{18}O$ and $\delta^{13}C$) from 7 stratigraphic levels, each corresponding to the laminated grainstones (lgA to lgE) and to the limestone breccia (br) at the top of the section (Fig. 2B).

The isotopic composition of bulk carbonates was measured at the Laboratory of Isotope Geochemistry of the Earth Sciences Department of Parma. To disentangle the calcite from the dolomite signals a selective acid extraction method has been used. About 40 mg of powdered bulk sample were reacted with >100% H_3PO_4 at 25 °C as follows in three steps: 1) for 2 h in vacuum to extract CO_2 from the calcite fraction, 2) continuously for 4 h in vacuum to obtain the calcite–dolomite mixture (CO_2 obtained in second step was pumping out from the system) 3) for >72 h for the dolomite fraction. The isotopic composition of the CO_2 collected during the three steps was measured on a Finnigan Delta S mass spectrometer and compared with the isotopic composition of an internal laboratory CO_2 standard gas of extra pure Carrara marble powder. The standard deviation of these measurements was regularly $\leq \pm 0.15‰$ (1σ). The CO_2 of the standard gas was periodically calibrated against NBS-19 revealing an isotopic composition of −2.43‰ ($\delta^{18}O$ vs.

VPDB) and + 2.45‰ ($\delta^{13}C$ vs. VPDB), respectively.

4. Results

4.1. New field observations and petrographic analyses on the Upper Metochia section (UMs)

We detailed the uppermost 10 m of the Metochia section (UMs), as described by Krijgsman et al. (2004), Drinia et al. (2007) and Zachariasse and Lourens (2021), recognizing a succession (Fig. 2B) of 14 lithological cycles, with a mean thickness of 50 cm. Up to cycle 11 they are tripartite and consist of i) organic-rich laminated shale (hereafter termed sapropel and sometimes described as laminated red clays in the literature), ii) laminated white diatomite and iii) massive grey micritic limestone. We noted that the massive limestone portion of the cycles can be very thin (cycle 3) or even absent (cycle 7, 9 and 13) and that in cycle 12 and from 14 upwards, it actually consists of laminated grainstone (Fig. 3e and f). The evident change of the limestone facies from cycle 12 (M130 of Zachariasse and Lourens, 2021) upward is described by all authors, as these layers became more prominent and characterized by more complex fabric and composition (bed lgA to lgF in Fig. 2B and Fig. 3D, E, F and G). The top of the section is represented by a limestone breccia of indetermined age, floored by an erosive surface.

While major differences are noted with respect to the description of Drinia et al. (2007), an overall agreement can be drawn between our UMs and the upper portion of the section as measured by Krijgsman et al. (2004) and by Zachariasse and Lourens (2021): i) 5 lithological cycles have been recognized between the thickest diatomite (our cycle 6, Fig. 2B and 3B; cycles M122 and M123 in Zachariasse and Lourens, 2021) and the first laminated grainstone (lgA); ii) below our cycle 6, two hybrid graded sandstone beds (in cycles 3 and 5) correlate with those in cycle M119 (top) and M121 of Zachariasse and Lourens (2021); it follows that cycle 1 of the UMs coincides with cycle M117. On the other side, differently from both previous works, we subdivided in two cycles the interval comprised between the first and second laminated grainstone (lgA and lgB, Fig. 2B and 3D, E and F).

The detailed petrographic observations of the basal laminar portion of the grainstone layer indicates that bed lgA is made up by a plane-parallel alternation of clotted micrite and clastic laminae, the latter including fine grained siliciclastic grains and microsparite with intraclasts, foraminifera, fish and other microfossil remains. Some of these laminae are broken-up forming a brecciated interval. Microsparite is sometime present as vertically oriented pseudomorphs after gypsum; these crystals are draped by the overlaying lamina. Towards the top of

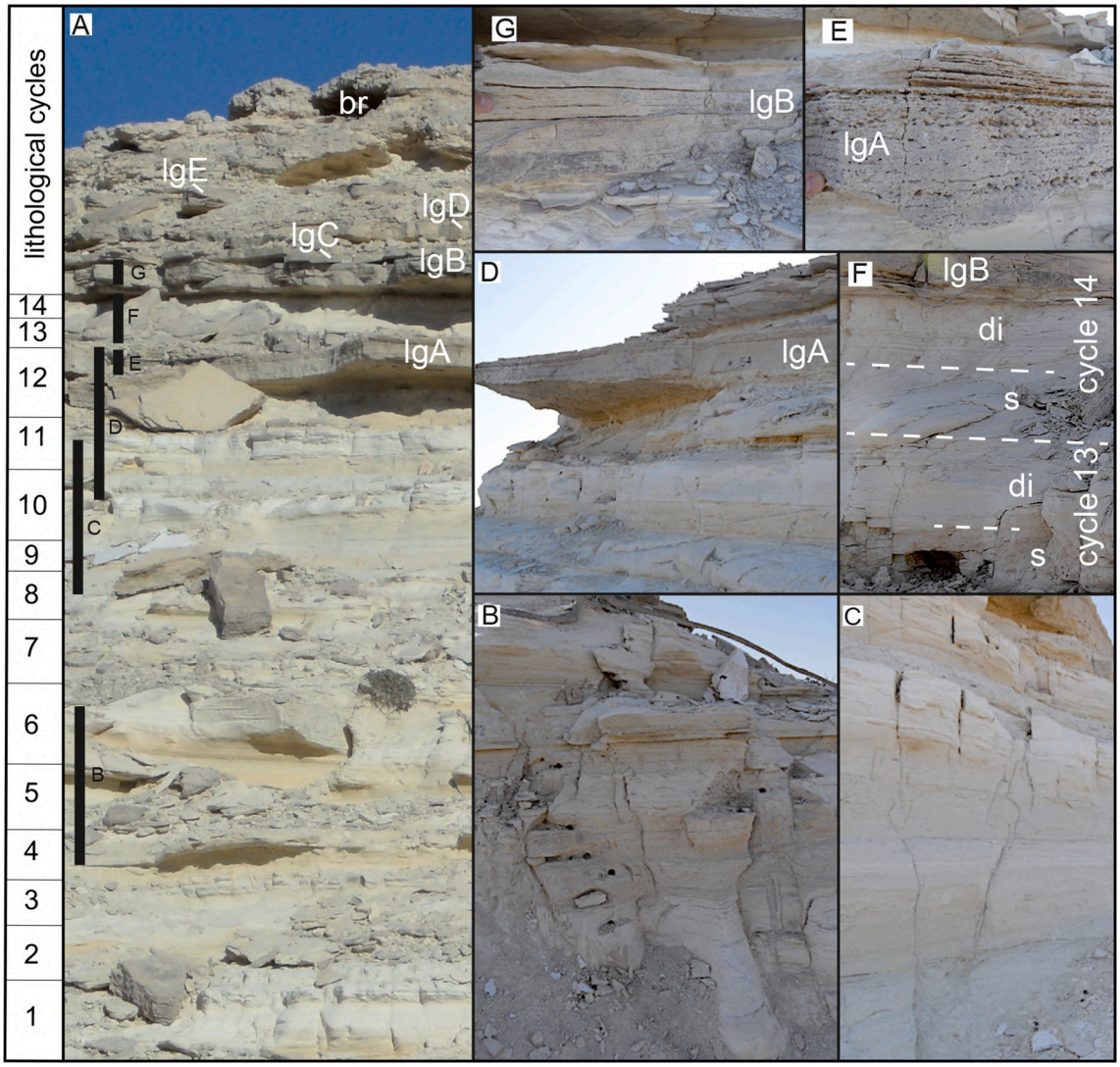

Fig. 3. Pictures of the upper Metochia section (A) and of selected stratigraphic intervals (B, C, D, E, F and G; see Fig. 2B). Also shown are the position of the prominent laminated grainstone (lgA, lgB, lgC, lgD and lgE), the brecciated carbonate (br) and, in picture E, the partition between sapropels (s) and diatomites (di) in cycle 13 and 14, which differs from the lithological log of Zachariasse and Lourens (2021), where only one cycle is described (M130 in Fig. 2A).

the bed, laminae are made up of large intraclasts and a fine grained, graded siliciclastic portion. Beds lgB, lgC, lgD and lgF also show an upper portion characterized by cross laminations (Fig. 3G). Bed lgB is a grainstone consisting of coated carbonate grains and intraclasts, commonly completely recrystallized, and containing a siliciclastic sand portion in its upper part. Bed lgC shows characteristics common to the basal portion of bed lgA and to the middle part of lgB; towards the top, it consists of a micrite rich in sponge spicules with foraminifera and fine siliciclastic grains. Bed lgD also starts as a laminite microspar, completely recrystallized, and ends with a micrite portion with graded foraminifer and sponge spicule clasts in the upper part. Beds lgE is also similar to the lower portion of bed lgA, but the microspar gypsum pesudomorphs are randomly oriented, indicating a displacive growth into mud. The section is topped by a limestone breccia (br in Fig. 3A) resting on an erosional surface and made up of clasts of laminated limestone with composition similar to that of bed lgA and with secondary gypsum crystals in the pore spaces.

4.2. Foraminifera

The abundances of planktic (PF) and benthic foraminifera (BF) show fluctuations that match the lithological cyclicity, with higher values generally corresponding to the uppermost part of the diatomites or the limestones (Fig. 4 and Table S1). From cycle 1 to 9 (0–5.4 m) several barren samples occur in cycle 2, 4, 5, 6 and 8; thus, a foraminifer reduction in abundance occurs (FR in Fig. 4). From cycle 9 upward, most samples are barren in the >125 μm fraction, except those in the sapropel of cycle 10 (rare PF and BF), in the limestone of cycle 11, sapropel of cycle 12 and sapropel of cycle 13. The uppermost two occurrences characterize the disappearance of the >125 μm PF (event 19p in Fig. 4) and BF (19b), respectively. However, in this upper interval and up to the topmost studied sample (above bed lgE), small bolivinids and *T. quinqueloba* occur in the 63–125 μm fraction in variable amount (not quantitatively evaluated).

The BF assemblages are largely dominated by *Bulimina aculeata* and *Bolivina* spp. (mainly *B. spathulata* and *B. dilatata*, rarely *B. dentellata* and *B. plicatella*); other less frequent taxa are *Elphidium*, *Neconorbina terquemi*, *Hanzawaia boueana*, *Valvulineria complanata* and *Oridorsalis stellatus*.

The PF assemblages, are usually oligotypic and dominated by different groups of taxa depending on the lithology (Fig. 4):

i) the limestones and lower part of the sapropel intervals mainly contain cold eutrophic PF assemblages (CE-PF; Sierro et al., 2003) with abundant or dominant *Turborotalita quinqueloba*, *T. multiloba* and the *Globigerinita* gr.
ii) the upper part of the sapropel commonly contain warm oligotrophic PF assemblages (WO-PF; Sierro et al., 2003), composed by *Orbulina universa* with minor amount of *Globigerinoides* gr., and *Globigerinella obesa*;
iii) the diatomite is dominated by *Neogloboquadrina acostaensis* with minor and variable amounts of the *G. bulloides* gr., and of the WO-PF *Globuturborotalita* gr. and *G. obesa*.

The PF vertical distribution along the section is characterized by well-defined patterns useful for stratigraphic purposes.

N. acostaensis is found in diatomitic intervals of cycles 2 to 4 and 6 to 8; the uppermost two occurrences are instead associated to the basal part of the sapropels of cycle 10 and 12. Its coiling is prevalently dextral, however, one influx of left coiled specimens (82% of left coiled over the

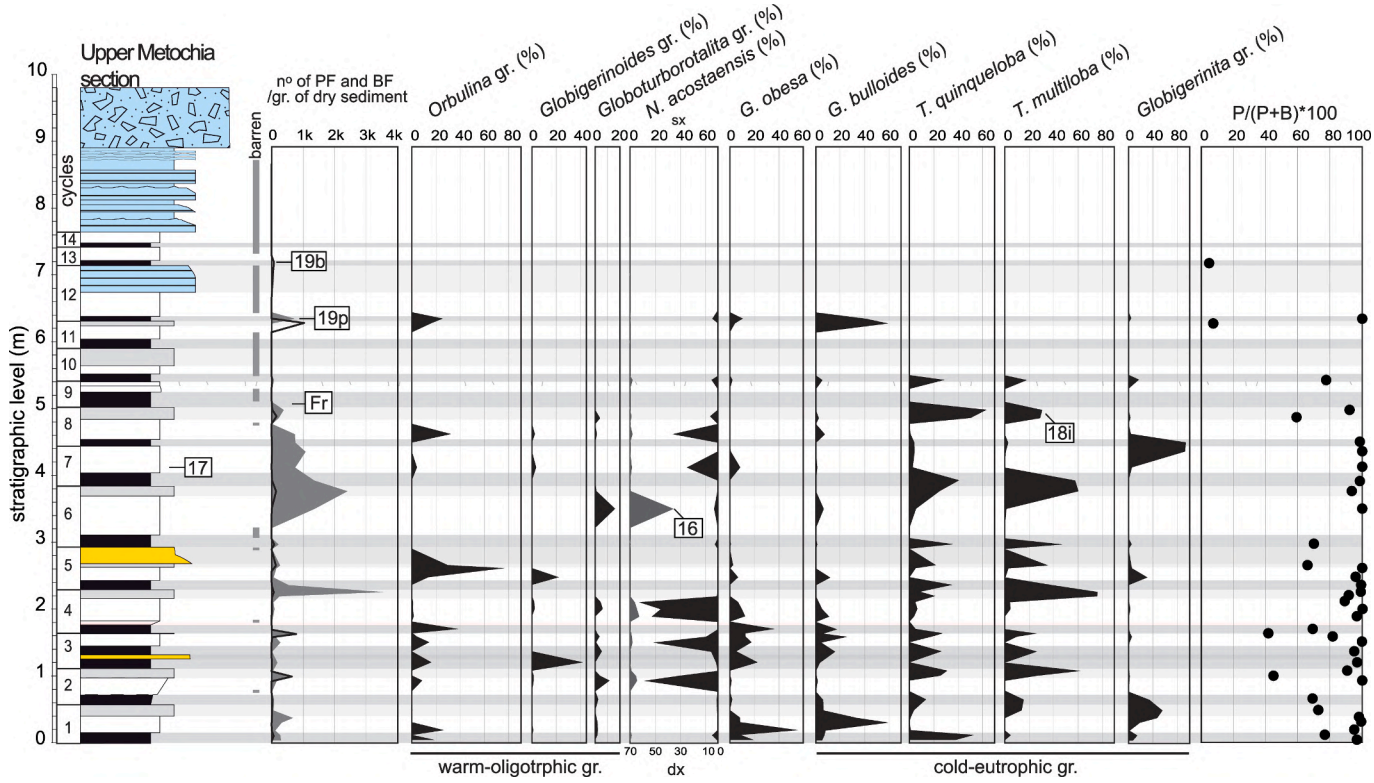

Fig. 4. Plots of benthic and planktic foraminifer total abundance (in n°/g of dry residue of benthic, black line, and planktic foraminifera, grey area), relative abundance (%) for each selected taxon and the planktic/benthic ratio. Grey vertical bars besides the log indicate interval with barren samples. Biostratigraphic events are: 16) influx of left coiled *N. acostaensis*, 17) influx of *Globorotalia scitula*, 18i) last influx of *Turborotalita multiloba*, FR) reduction in frequency of foraminifera, 19p) disappearance of planktic foraminifera (PFD) and 19b the disappearance of benthic foraminifera (BFD). Right coiled *N. acostaensis* % (in black and increasing from right to left) and left coiled *N. acostaensis* % (in grey and increasing from left to right) are shown in the same plot. On the bottom of the plots, warm-oligotrophic planktic and cold-eutrophic groups are indicated.

total neogloboquadrinids, event 16 in Fig. 4) occurs in the upper part of the diatomite of cycle 6. A second, minor influx occurs in the sapropel of cycle 10 (30%), but it is associated to a low total neogloboquadrinids abundance (7.34%, see supplementary material). The *Globigerinoides* gr. is generally absent or rare, and only shows two abundance peaks in the sapropel of cycle 3 and at the base of the diatomite in cycle 5. The *G. bulloides* gr., *O. universa*, the *Globigerinoides* and *Globoturborotalita* groups and *G. obesa* are more frequent in the lower part of the section up to about 3 m, from where turborotalids increase in abundance. *T. multiloba* and *T. quinqueloba* occurs together and commonly make up almost the entire PF assemblage. *T. multiloba* pattern is characterized by influxes characterized by relative abundances from 20% to almost 80% (top cycle 4); the last influx (18i in Fig. 4) is recorded at the top of cycle 8 and the last occurrence at the base of cycle 10 (Fig. 4).

The P/B ratio (Fig. 4) is generally high (70 to 100%) indicating the prevalence of planktic on benthic foraminifera, except in the limestone layers of cycle 1 to 3, 5, 8 and 11, where the P/B values are lower than 70%, with a minimum in cycle 10 (10%). The BF and PF assemblages do not show significant changes in relation with the P/B ratio.

4.3. Calcareous nannofossils

Calcareous nannofossils (CN) are very abundant along the UMs, with highest abundance centered in the sapropels and marls and lowest in the diatomite, which are more pronounced from cycle 6 upward (Fig. 5 and Table S1). Small *Reticulofenestra* (<5 μm) are usually the predominant component of the assemblage, with evident minima in the sapropels or diatomite bases only from cycle 4 upward. From the base up to cycle 8, total CN abundance is in phase with the relative abundance of the Small *Reticulofenestra* (<5 μm); from cycle 10 this phase relation is inverted, and CN abundance is in antiphase with the Small *Reticulofenestra* (<5 μm). This change coincides with the onset of prominent abundance peaks of the *Sphenolitus* spp. in the sapropels/lower part of the diatomites. *Calcidiscus leptoporus* is common to abundant in the marl/sapropel transition from cycle 4 to 7, with peaks up to 75%. *Helicosphaera carteri*, *Umbilicosphaera rotula* and *Umbilicosphaera jafari* are all characterized by prominent but discontinuous abundance peaks with no obvious preference for any lithology. Abundance peaks of the *Sphenolitus* spp. (pSp in Fig. 5), *H. carteri* (pHc in Fig. 5) and *U. rotula* (pUr) are present in the sapropel/diatomite of cycle 13, sapropel of cycle 14 and diatomite of cycle 14. Another peculiar pattern is the short acme of *Reticulofenestra perplexa* in cycles 9 to 11 (abR and aeR in Fig. 5), with a maximum centered in the marl of cycle 10. The occurrence of *Braarudosphaera bigelowi* in a single sample at the marl/sapropel transition between cycles 4 and 5 is also worth noting (iBb in Fig. 5).

4.4. Strontium and stable isotopes

The $^{87}Sr/^{86}Sr$ values of the UMs on PF assemblages or bulk rock samples in levels characterized by scarce or absent specimens of foraminifera show similar values, with few exceptions (samples from sapropels of cycles 1 and 6), these two types of samples, show similar values (Fig. 6A).

Over the 95% of the values are comprised in a narrow interval between 0.708999 ± 0.000008 and 0.708894 ± 0.000014 (Fig. 6B; Table S2).

Considering the average values calculated for each lithology (Fig. 6): i) the lower values are generally observed in the diatomites or sapropels and higher values in the limestones; ii) sapropel, and secondarily diatomites values also show broader variability (and standard deviation or error). In the lower part of the section, the variation of $^{87}Sr/^{86}Sr$ from one sample to the successive is commonly so small that it falls within the

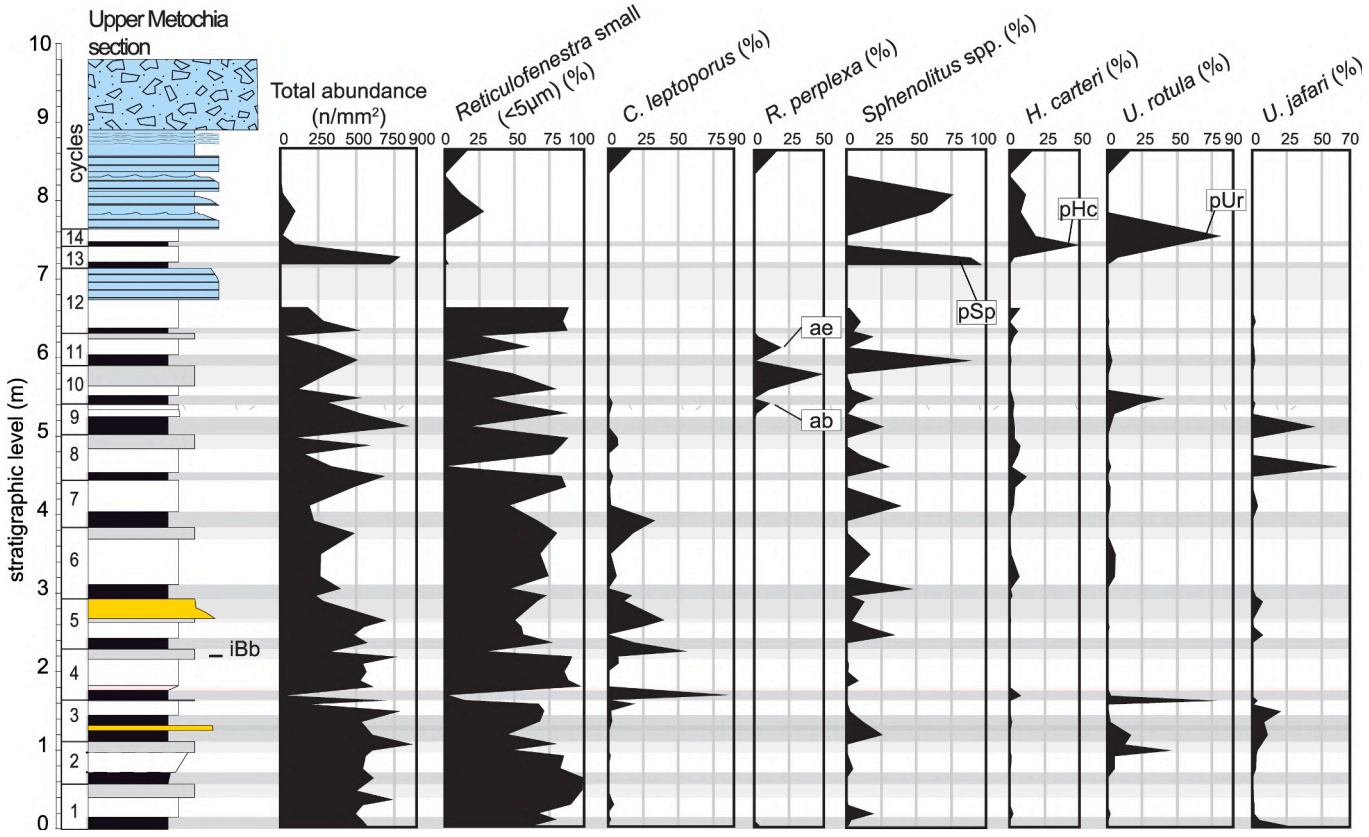

Fig. 5. Plots of calcareous nannofossils total abundance (n/mm^2) and relative abundance (%) of the selected taxon. The following bioevents are indicated besides the log and the plots: *B. bigelowi* influx (iBb); acme beginning and end of *R. perplexa* (abR and aeR, respectively); the MSC onset bioevents (Lozar and Negri, 2019), composed of the peaks of the *Sphenolitus* spp. (pSp), *H. carteri* (pHc) and *U. rotula* (pUr).

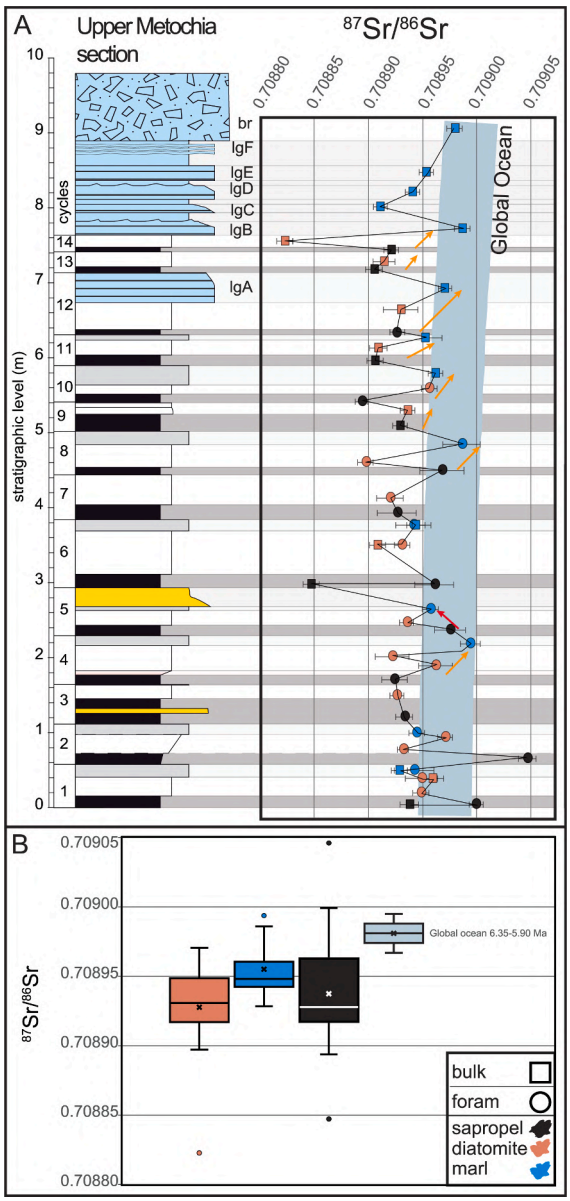

Fig. 6. A: Plot of the $^{87}Sr/^{86}Sr$ against stratigraphic level for sapropels (black), diatomites (light red) and limestones, grainstones and breccia (light blue), as calculated from bulk rock samples (squares) and foraminifera (circles). Arrows depict indicative trends within each cycle, as discussed in the text. The Global Ocean curve (McArthur et al., 2012) is plotted for reference in light blue. B: Boxplots showing the variability of the $^{87}Sr/^{86}Sr$ for the UMs samples (both bulk and foraminifer samples). Outliers are indicated as circles. Global Ocean values are retained from McArthur et al. (2012). (For interpretation of the references to colour in this figure legend, the reader is referred to the web version of this article.)

error bar, producing no significative changes (Fig. 6A). Upward (cycles 4 and 5, and from cycle 8), values are more dispersed and variation within the cycles are more significant. Thus, different trends can be described within each cycle: in the lowermost seven cycles no significant variation or a slightl decrease in values from the bottom (sapropel) to top (limestones) is observed; in cycle 4 and from cycle 8 upward the trend is markedly increasing from the bottom to the top of the cycles (Fig. 6B).

The switch between no or decreasing trend to the increasing trend is the result of a long-term variation which can be observed in a stratigraphic order in the three lithologies taken together or separately (Fig. 6A). Starting from the base of the section, sapropel and diatomite values are characterized by a depletion trend diverging from those of the limestones (Fig. 6A), which themselves remain within the Global Ocean curve (McArthur et al., 2001, 2012) up to bed lgB (Fig. 6A). Above this level, the laminated grainstones show a slight depletion trend and the laminated bed lgB, lgC and lgD show values similar to those of the uppermost sapropels and diatomites (cycle 13 and 14). The brecciated carbonate (br) finally returns within the Messinian Global Ocean values.

Oxygen and carbon stable isotope were quantified on bulk samples of the laminated grainstones of the upper part of the section (Fig. 7). The $\delta^{18}O$ values show a low dispersion from −1.72 to 0.99 ‰ and the $\delta^{13}C$ from −4.84 to −1.34 ‰. Bed lgA and lgC show very similar light $\delta^{18}O$ (ca. -1.7 ‰) and $\delta^{13}C$ values (−3.79 and − 4.84 ‰, respectively). The other layers have progressively heavier values, with $\delta^{18}O$ of bed br being close to 1 ‰ and $\delta^{13}C$ of bed lgE −1.34 ‰.

5. Discussion

5.1. Age model and calibration of calcareous nannofossil bioevents

The abundance of *T. quinqueloba*, the occurrence of *T. multiloba* and the predominance of right coiled *N. acostaensis*, all from the base of the UMs (Fig. 4), indicate that the interval up to the disappearance of planktic foraminifera can be assigned to the MMi13d subzone of Lirer et al. (2019). Within this subzone three age calibrated planktic foraminifer events (Sierro et al., 2001; Lirer et al., 2019) are recognized (Fig. 8): the 1st influx of left coiled *N. acostaensis* (6.125 Ma, event 16 in cycle 6 in Fig. 8), the 2nd influx of *G. scitula* (6.102 Ma, event 17 in cycle 7) and the last influx of *T. multiloba* (6.07 Ma, event 18i in top cycle 8). The planktic foraminifer biostratigraphy is very similar to that presented in Zachariasse and Lourens (2021); the main differences regards the second influx of left coiled neogloboquadrinids (event 18 at Perales and Falconara, see Fig. 8) that was not recognized by our quantitative analyses, possibly because of its very short duration and/or a different sampling rate or position of the samples.

Consequently, our age model (Fig. 9) confirms that of Zachariasse and Lourens (2021), including the new age for the lowermost grainstone layer (bed lgA), previously considered the local expression of the MSC onset with an age of 5.96 Ma (Krijgsman et al., 2004), and then dated at 6.00 Ma (Fig. 9). In respect to the age model of Zachariasse and Lourens (2021) few remarking discrepancies in the lithological log are worth noting: i) our thick cycle 6 can be interpreted as a double cycle (as in Krijgsman et al., 2004), ii) the thick double cycle M130 of Zachariasse and Lourens (2021) can be split in cycle 13 (lacking the limestone partition due to weak insolation), corresponding to an eccentricity minimum lacking the insolation minimum, and cycle 14 (Fig. 8).

The age model provides astronomical age for the calcareous nannofossil bioevents of the uppermost pre-evaporitic phase (Fig. 9). The *B. bigelowi* influx in the marl of cycle 4, found in a coeval level of the Tokhni section (Cyprus, Manzi et al., 2016; Gennari et al., 2018) has an

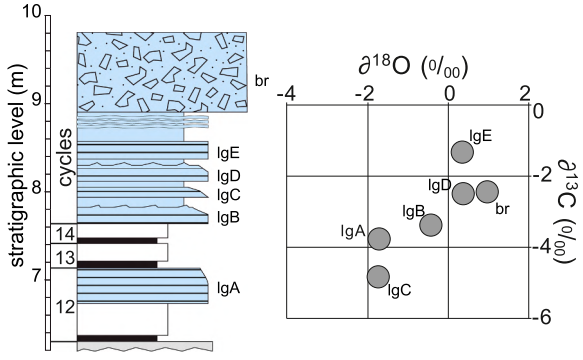

Fig. 7. $\delta^{18}O$ and $\delta^{13}C$ of bulk rock samples collected in the prominent laminated grainstone beds (lgA, lgB, lgC, lgD, lgE) and in the limestone breccia (br) of the upper portion of the UMs.

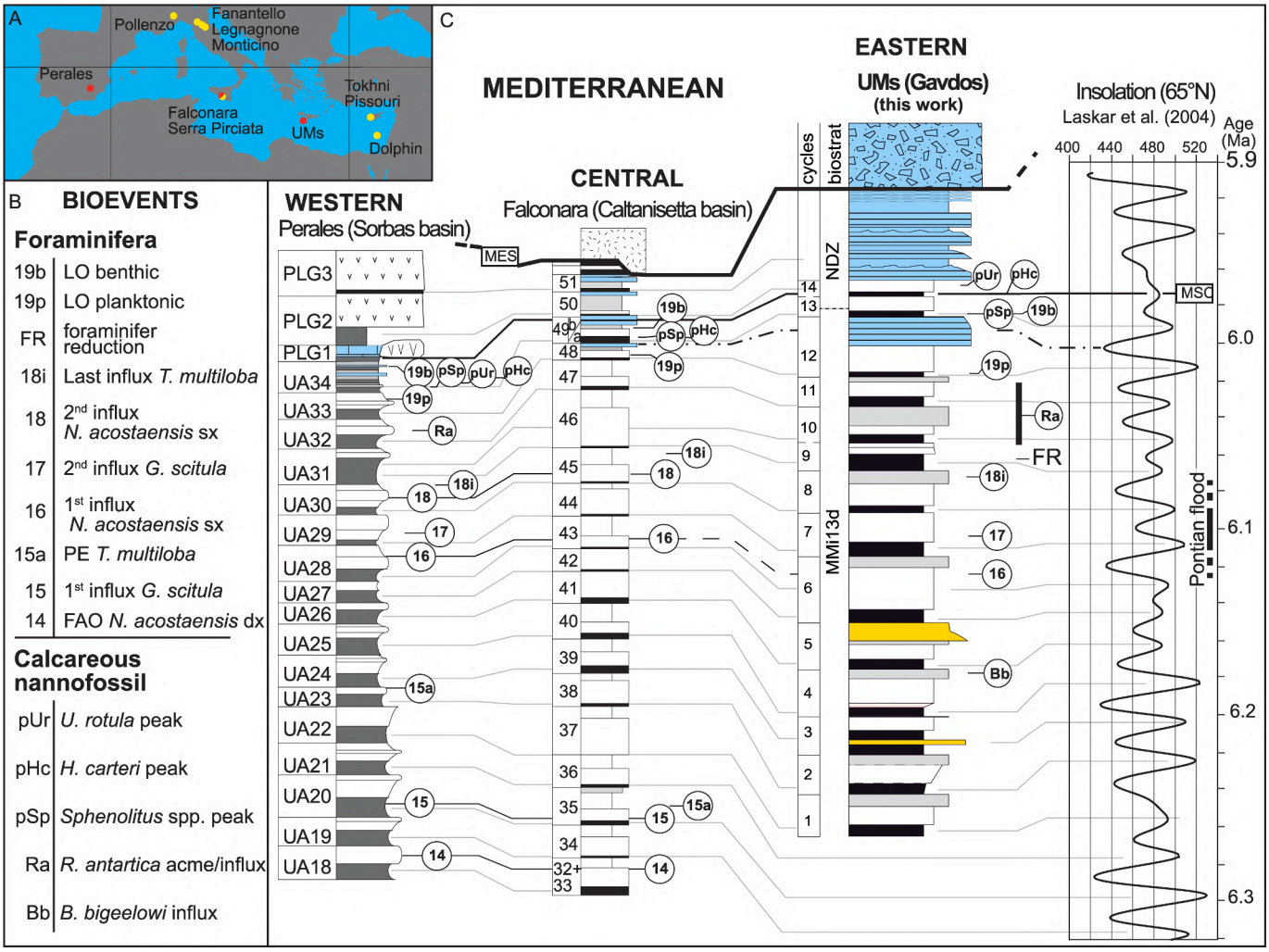

Fig. 8. A: In red, location of the UMs and the western and central Mediterranean reference Perales (Sorbas Basin; Sierro et al., 2001; Manzi et al., 2013; Mancini et al., 2020) and Falconara (Caltanisetta basin; Blanc-Valleron et al., 2002; Hilgen and Krijgsman, 1999; Manzi et al., 2011; Lozar and Negri, 2019) sections, used for the correlation panel (this figure). In yellow, location of the sections compared in Fig. 11. The thickness of limestone of the upper part of the Falconara section (light grey) has been exaggerated for better visibility. B: Calcareous plankton bioevents correlated throughout the three sections (FAO = first abundant occurrence, PE = paracme end, LO = last occurrence). C: Correlation between the Perales, Falconara and Upper Metochia sections and with the 65°N summer insolation curve (Laskar et al., 2004); MES is the Messinian erosional surface and MSC is the Messinian salinity crisis onset, respectively. Biostratigraphic zones beside the UMs from Lirer et al. (2019). (For interpretation of the references to colour in this figure legend, the reader is referred to the web version of this article.)

age of 6.17 Ma (Fig. 9). An acme (max relative abundance 50%) of *R. perplexa* (*R. antarctica* in Gennari et al., 2018) occurs in the massive limestones of cycles 9, 10 and 11, from ca. 6.058 to 6.018 Ma (Ra in Figs. 8 and 9), above the last influx of *T. multiloba*. The same acme is also recorded in the Tokhni section (ca. 6.04 to 6.02 Ma; Gennari et al., 2018), where the younger base is probably caused by the occurrence of a conglomeratic bed with an erosive base. Only a short influx (ca. 50%) is present in the diatomites of cycle UA32 of the Perales Section (Fig. 8; Mancini et al., 2020), with an age of ca. 6.02 Ma, which would correspond to the top of the acme in the UMs.

Among the CN MSC onset bioevents (Figs. 8 and 9) that best approximate the beginning of the crisis (Manzi et al., 2007, 2018, 2021; Lozar and Negri, 2019; Mancini et al., 2020), an age of ca. 5.990 Ma was calculated for the peak of *Sphenolitus* spp. (sapropel of cycle 13) (Figs. 8 and 9) and 5.973 Ma (sapropel of cycle 14) for the peak of *H. carteri*, slightly followed by that of *U. rotula* (ca. 5.968 Ma, in the diatomite of cycle 14) (Figs. 8 and 9).

5.2. Anatomy of the pre-evaporitic lithological cycles

The lithological cycles of pre-evaporitic successions (7.16–5.97 Ma) deposited in the Mediterranean are explained by variation of the insolation index, with maxima conventionally correlated to sapropel mid-points (Hilgen et al., 1995; Krijgsman et al., 2004; Marzocchi et al., 2015; Simon et al., 2017). Based on paleoceanographic proxies, Sierro et al. (2003) and Mancini et al. (2020) proposed to correlate insolation maxima to the sapropel/lower marl transitions of the Sorbas Basin, when WO-PF and *S. abies* indicate maximum SST and stratification. Perez-Folgado et al. (2003) proposed an alternative idea for the Eastern Mediterranean with the insolation maxima are tuned to the diatomite mid-point of the Gavdos cycles, based on the occurrence of diatoms and *N. acostaensis* thriving in the Deep Chlorophyll Maximum (DCM). Differently, we suggest a common Mediterranean phase relation among lithological cycles and insolation. The new UMs CN data document the occurrence of *S. abies* at the sapropel/diatomite transitions at Gavdos (coinciding with WO-PF peaks, Fig. S4), a pattern already observed at Sorbas (Mancini et al., 2020) indicative of the establishment of a lower photic zone productivity below oligotrophic and warm surface waters during periods of stratification triggered by runoff and warming at insolation maxima.

The lack of Deep Chlorophyll Maximum (DCM) diatoms and Neogloboquadrinids in the sapropelitic sediments is rather explained by the

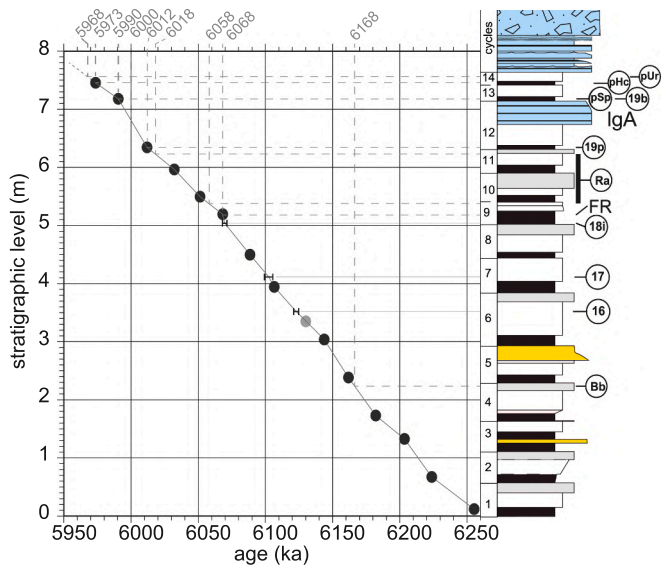

Fig. 9. Age model for the UMs section. Insolation maxima (black dots) corresponding to the mid-point of sapropels and selected foraminifer bioevents (16, 17 and 18i), as dated by Sierro et al. (2003) and Lirer et al. (2019), were used as tie points. Bioevent labels as in Fig. 9B. The proposed age for the other bioevents graphically calculated based on linear interpolation of the sedimentation rate between two successive insolation maxima. These ages are shown in grey on the top scale of the age model. The missing insolation maximum of the double cycles 6 (thick diatomite indicated with a black bar) is displayed as a grey dot.

high siliceous dissolution rates in anoxic bottom waters (Pellegrino et al., 2018) and warm temperature (Sierro et al., 2003), respectively. We also observe that the occurrence of *S. abies* peaks during each insolation maxima is only typical of Southern Mediterranean successions from east to west (Gennari et al., 2018; Mancini et al., 2020; this work), probably in response to a south-to-north sea surface temperature gradient.

Successively, diatomites formed during decreasing insolation and temperature, leading to maximum seasonality (Mancini et al., 2020) and promoting the shallowing of the pycnocline or a seasonal disruption of the stratification (Sierro et al., 2003; Flores et al., 2005; Gennari et al., 2018). This configuration allowed to maintain high productivity both in the upper and lower photic zone and fueled the siliceous productivity (Filippelli et al., 2003).

The low and statistically undistinguishable $^{87}Sr/^{86}Sr$ isotope values among sapropels and diatomites (Fig. 6A and B) is a prerogative of the UMs and different from the Sorbas Basin, where diatomite have higher values (Modestou et al., 2017; Reghizzi et al., 2017). As climatic models predict high African monsoon activity and runoff only at insolation maxima (Marzocchi et al., 2015), the prolonged Sr perturbation in the UMs diatomites suggests that the slow recovery was due to a more severe restriction in the Eastern Mediterranean, close to the African runoff input. The possible occurrence of additional intermittent input from the Paratethys (Vasiliev et al., 2013) can be eventually envisaged, but, at the moment, no further independent data may confirm or discard this hypothesis.

The proximity to the African continent, which experienced a major C_3 to C_4 plant shift during the Late Miocene (Pellegrino et al., 2018) and the restricted circulation, also contributed to increase the Si reservoir in the Eastern Mediterranean, explaining a prolonged diatomite deposition (Pestrea et al., 2002; Saint Martin et al., 2003; Mansour et al., 2008). Differently, in the Western and Northern Mediterranean diatomites are thinner and separated from the sapropel by a marl intercalation (Sierro et al., 2003) or absent (Kouwenhoven et al., 2003; Manzi et al., 2007; Dela Pierre et al., 2011; Gennari et al., 2013), respectively.

A homogeneous scenario is instead characteristic of the periods of insolation minima, when lower runoff and decreasing temperatures allowed the reprisal of the thermohaline circulation and the coupling of the Mediterranean $^{87}Sr/^{86}Sr$ values with the Global Ocean. During insolation minima most basins record increasing surface productivity, predicted by surface water eutrophic PF and CN (Blanc-Valleron et al., 2002; Sierro et al., 2003; Gennari et al., 2018; Mancini et al., 2020). As in the Sorbas Basin (Mancini et al., 2020), the high productivity typical of the massive limestones perdured and possibly increased at the sapropel inception. Like in the modern oxygen minimum zones (Schumacher et al., 2007; Schimmelmann et al., 2016), this process stimulated high organic carbon export to the seafloor, low bottom water oxygen levels and allowed reaching the tipping point of organic matter preservation. A low runoff contribution, suggesting that stratification was not the main trigger of organic matter preservation at the sapropel inception, is indicated by high values, within the Global Ocean range of the $^{87}Sr/^{86}Sr$ values at the base of sapropels of cycles UM1, 2, 5, 6 and 8 (Fig. 6).

5.3. *The uppermost pre-evaporitic events from an Eastern Mediterranean perspective*

The age model and the phase relation between insolation and lithological cycles of the UMs allow to discuss the trends and events that closely preceded and marked the MSC onset, as revealed by the multiple proxy dataset here presented.

5.3.1. *Hydrographic changes from 6.2 to the MSC*

The Mediterranean was already subjected to restriction since the early Messinian due to the tectonic reorganization of the gateways area (Krijgsman et al., 1999; Kouwenhoven et al., 2006; Capella et al., 2019; Ng et al., 2021; Bulian et al., 2022; Kontakiotis et al., 2022). Despite the slowing down of the thermohaline perturbation, the surface oceanic inflow into the Mediterranean was apparently intact as indicated by the $^{87}Sr/^{86}Sr$ values within Global Ocean range during most of the pre-evaporitic phase. Short living isolation events are suggested by Flecker and Ellam (2006) and excursion of the $^{87}Sr/^{86}Sr$ to lower values occur in few intervals at high insolation during some eccentricity maxima at 6.4, 6.3 and 6.1 Ma (Reghizzi et al., 2017; Modestou et al., 2017), before the final divergence, after 6.0 Ma and during the MSC (Reghizzi et al., 2017; Gennari et al., 2018; Manzi et al., 2021). However, the pre-evaporitic Mediterranean $^{87}Sr/^{86}Sr$ record was focused on the long-term trend and the precession variability was overlooked. The precessional scale resolution from 6.25 Ma to the earliest MSC phase obtained for the UMs allows for the first time to observe the progression of the $^{87}Sr/^{86}Sr$ values associated to the insolation, as expressed in the three lithologies composing the sedimentary cycles (Fig. 10). The affinity for oceanic values of the marls and lgA (insolation minima) is consistent through time up to the laminated grainstone B at ca. 5.96 Ma (i.e. the line has an increasing upward trend; see Fig. 10C), similarly to what observed on Cyprus (Eastern Mediterranean, Gennari et al., 2018). Differently, diatomites and sapropels show a clear depleting upward trend towards values progressively lower than the Global Ocean (Fig. 10A and B). This divergence started at 6.2 Ma, indicating that at least from this interval, during insolation maxima and shortly after it (diatomite), the amount of Atlantic waters entering the Central/Eastern Mediterranean decreased relatively to the input of continental waters and the hydrography started to oscillate between increasingly different conditions from insolation minima to maxima.

Among the mechanisms controlling the proportion of Atlantic and runoff waters residing in the Mediterranean, the onset of Northern Hemisphere glaciations (Holbourn et al., 2018), the tectonic restriction of the gateways, increasing runoff and a more efficient Mediterranean/Paratethys connectivity could be considered. Although a prominent glaciation do not coincide with the MSC onset (Krijgsman et al., 2004), the marine oxygen isotopic record from 6.2 to 6.0 Ma (Van der Laan

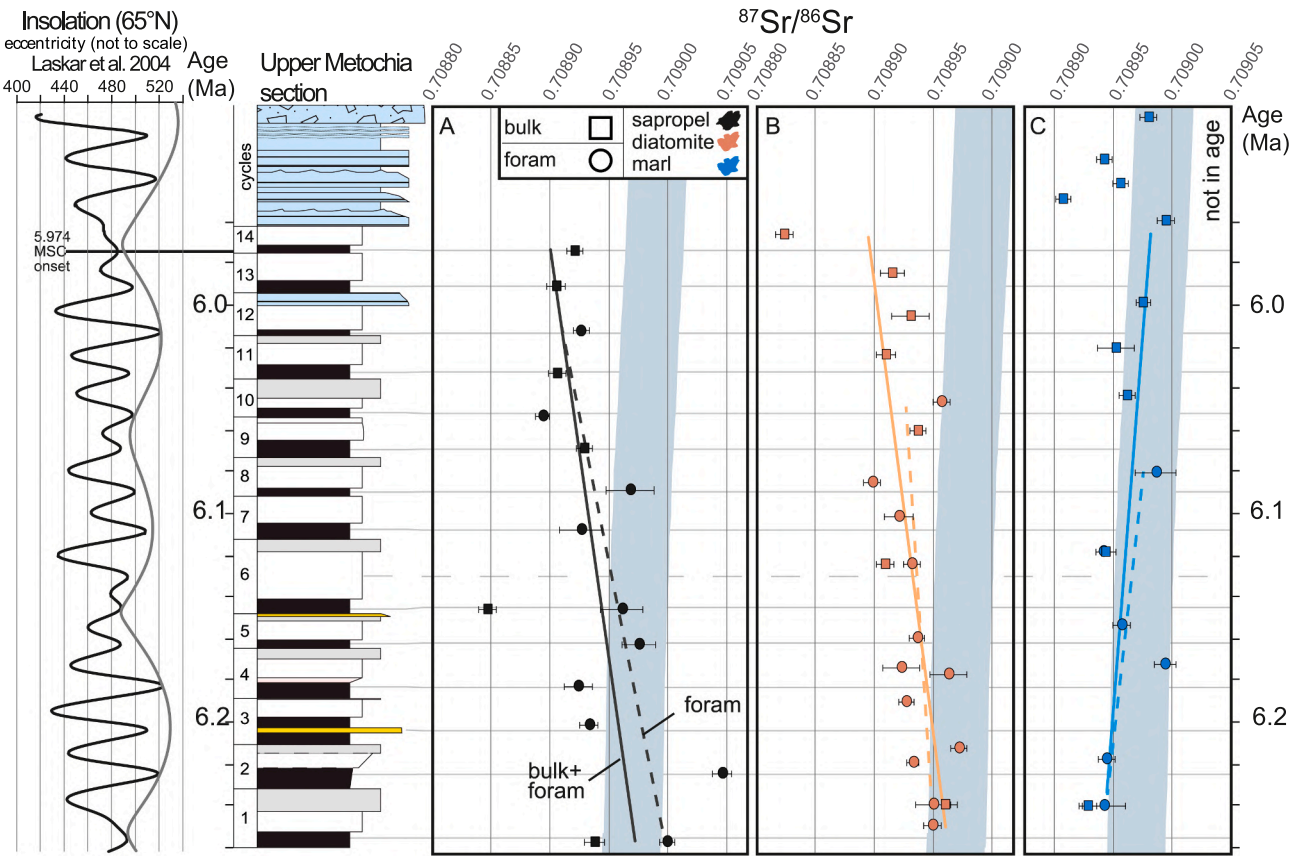

Fig. 10. Plots of the $^{87}Sr/^{86}Sr$ data against the age model of the UMs; for each lithology (A, sapropels; B, diatomites and C, marls, laminated grainstones and breccia) the linear trends are calculated and shown for foraminifer samples (dashed) and for foraminifer and bulk samples together (bold). For the marls and laminated grainstones two different trend lines were calculated for cycles 1 to 12 and for the interval above 7.6 m (lgB and successive beds), respectively.

et al., 2005) is characterized by progressively more prominent glacial stages associated to a long-term sea-level fall (Miller et al., 2011), indicating a further shallowing of the Atlantic gateway, following those at 7.2 and 6.8 Ma, suggested by salinity-based simulation (Krijgsman et al., 2018). A moderate eustatic sea level fall, in the order of 20 m (Simon and Meijer, 2015), could have been coupled with tectonic activity. Although a precise chronology of the tectonic events in the gateways area is hindered by the uplift and erosion of the sedimentary successions before the uppermost pre-evaporitic phase (Capella et al., 2018; Krijgsman et al., 2018), evidence of tectonic activity in the peri-Mediterranean area is documented between 6.3 and 6.1 Ma (roughly coinciding with the long-term eustatic fall), with increasing sedimentation rate and sedimentary instability in the Northern Apennine foredeep (Manzi et al., 2007), in Piedmont (Violanti et al., 2013; Gennari et al., 2020), on the Ionian Islands (Karakitsios et al., 2017), in the Sorbas Basin (Sierro et al., 2001) and on Cyprus (Krijgsman et al., 2004; Gennari et al., 2018).

The increase of the Mediterranean runoff started during the Late Miocene humid phase and was triggered by larger than modern discharge from the monsoon-fed African rivers (Griffin, 2002; Griffin, 2006; Gladstone et al., 2007, Holbourn et al., 2018). This runoff component is synchronized with insolation maxima and is especially stronger during eccentricity maxima (Simon et al., 2017). However, the sea surface water freshening from high (45 psu) to normal marine values (ca. 39 psu) in the Central Mediterranean Kalamaki section (Ionian Islands; Vasiliev et al., 2019; see also Kontakiotis et al., 2022) is an independent evidence that additional increasing continental water influence on the Mediterranean water body occurred after 6.2 Ma. For instance, slowing down of the deep-water formation due to increasing fresh water input favored stratification, that was inherited during the MSC, when it played a role in the evaporite precipitation (Simon and Meijer, 2017). The 6.2 Ma Mediterranean freshening is immediately followed by the "Pontian flood", an event of increased Mediterranean/Paratethys connection, roughly dated at 6.1 Ma (Vasiliev et al., 2013; Fig. 8). While the income of Mediterranean waters in to the Paratethys is well documented (Stoica et al., 2013; Grothe et al., 2020), the opposite is difficult to prove and the depleted values of the Mediterranean $^{87}Sr/^{86}Sr$ is best explained with increased runoff. However, a more efficient connection could have contributed to the $^{87}Sr/^{86}Sr$ trend, although evidence of a consistent and prolonged connection is only recorded later, during the Lago-Mare phase, when a large 87Sr/86Sr drop occurred (Roveri et al., 2014b) and when paratethyan fossil immigrants entered the Mediterranean (Orszag-Sperber, 2006).

A second hydrographic change, recognized in the Tokhni section just before the MSC onset (Cyprus, Gennari et al., 2018), occurred in the UMs at ca. 5.96 Ma (Fig. 10C); it is characterized by a decrease of $^{87}Sr/^{86}Sr$ values in the laminated grainstones, with diverging path from the global oceanic field, suggesting that the gateway restriction limited the Atlantic inflow to a threshold that hindered the compensation of the weak runoff contribution at time of insolation minima. This second step represents the inception of a permanent restricted circulation that became progressively more evident during the first and second stages of the MSC (Roveri et al., 2014b; Reghizzi et al., 2018) and culminated during the Lago Mare phase (Marzocchi et al., 2015).

5.3.2. *The response of calcareous plankton to hydrographic changes*

5.3.2.1. Foraminifera. The hydrographic change from 6.2 Ma is coupled with variations of the micropaleontological record. The divergence from oceanic values of the $^{87}Sr/^{86}Sr$ ratio from 6.2 Ma is coeval with a

reduction of the WO-PF group, except *O. universa*, and an increase in abundance and dominance of turborotalids among the CE-PF (Fig. 4). The increase of *O. universa*, replacing the *Globigerinoides* gr. is also recorded in the Sorbas Basin (Sierro et al., 2003). Both *O. universa* and *T. quinqueloba* can thrive in a wide range of environments, as indicated by the ubiquitous ecology of their modern representatives (Darling and Wade, 2008). In particular, modern *O. universa* genotypes are found in both oligotrophic and eutrophic environments, at variable temperatures (Morard et al., 2009). *T. quinqueloba* is adapted to a wide range of marine salinities (Kroon et al., 1988; Aksu et al., 2002; Ijiri et al., 2005) and proliferates in eutrophic and preferentially cold waters (Schiebel and Hemleben, 2017; Melki et al., 2010). The increase of these two PF taxa matches well the increment of environmental variability associated to the variation of the $^{87}Sr/^{86}Sr$ with precession.

Successive important changes are then represented by the reduction of foraminifer abundance (FR) and the frequency increase of levels barren of foraminifera >125 μm from cycle 9 (ca. 6.068 Ma), well before their disappearance (FD) in cycle 13 (ca. 5.990 Ma) (Fig. 9). Although obtained with either a quantitative or qualitative method, the FR prior to their disappearance is consistently recorded in many Eastern and Central Mediterranean successions (Blanc-Valleron et al., 2002; Kouwenhoven et al., 2006, Gennari et al., 2018; Manzi et al., 2018, 2021; Fig. 11) and in the Fanantello borehole in the Northern Mediterranean (Manzi et al., 2007), all characterized by the absence of primary gypsum of the PLG unit. Differently, a single-step, sharp FD closely predating the MSC onset was documented in the Perales section of the Sorbas Basin

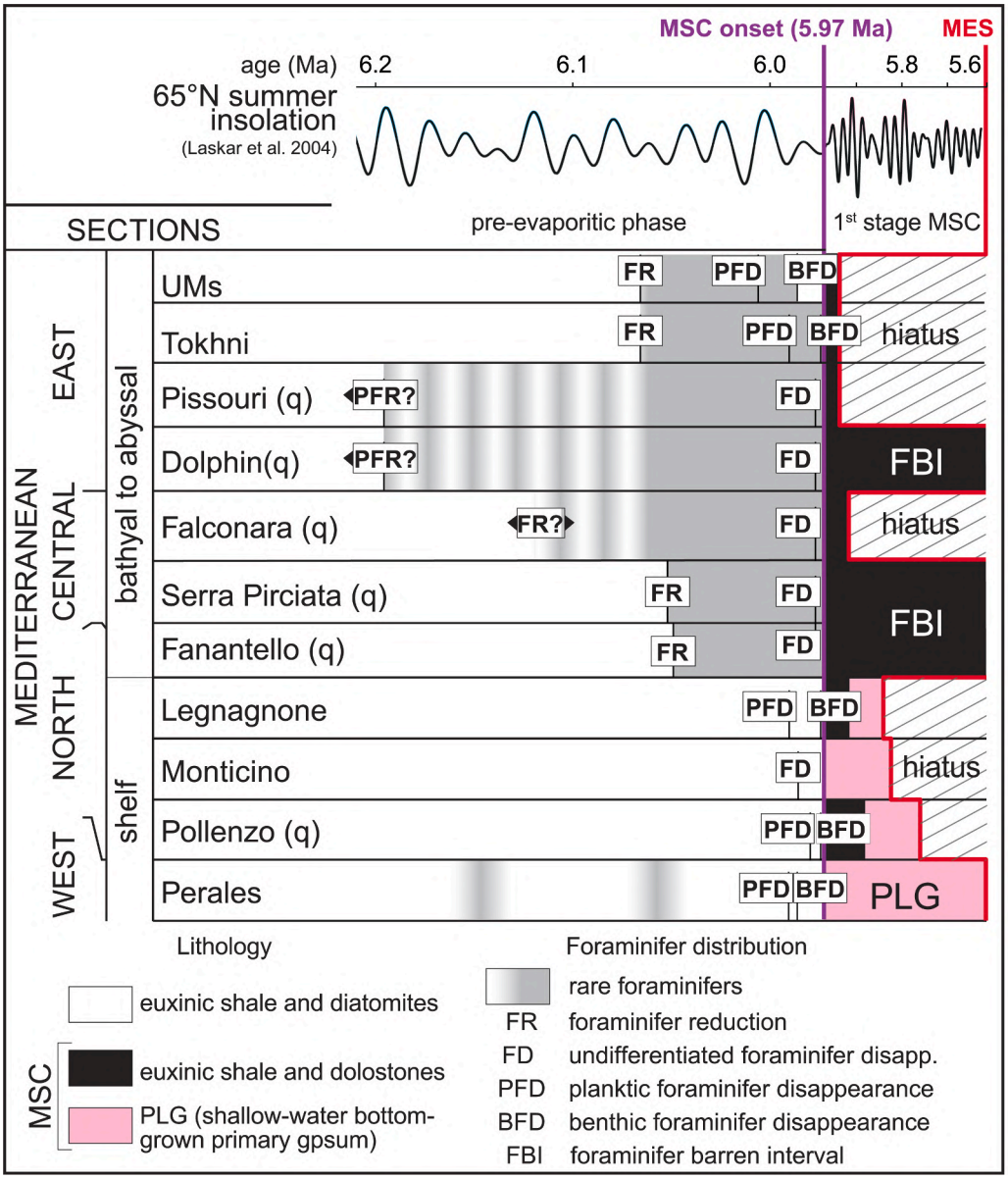

Fig. 11. Pattern and chronology of foraminifer reduction (FR) and disappearance (PFD, planktic; BFD, benthic; FD, undifferentiated) throughout the Mediterranean. The letter q beside the name of the sections indicates that only qualitative estimation on total foraminifer abundance is available. Sections are ordered from top to bottom according to their geographic position within the Mediterranean and depositional setting. On the right side of the figure, the different patterns of foraminifer reduction and disappearance are compared to the stratigraphy of the MSC deposits for each section; the presence of the PLG unit or of time-equivalent evaporite-free foraminifer barren interval is evidenced (FBI, Manzi et al., 2018, 2021), while the red line represents the Messinian erosional surface. Data are collected from this work and from Blanc-Valleron et al. (2002), Sierro et al. (2003), Kouwenhoven et al. (2006), Manzi et al. (2007), Riforgiato et al. (2008), Manzi et al. (2011), Gennari et al. (2013), Lozar et al. (2018), Manzi et al. (2018, 2021). (For interpretation of the references to colour in this figure legend, the reader is referred to the web version of this article.)

(Mancini et al., 2020) and in Central/Northern Italy at Gello (Riforgiato et al., 2008), Legnagnone (Gennari et al., 2013) and Pollenzo (Violanti et al., 2013), where primary bottom-grown gypsum of the PLG unit accumulated. Among this group, only in the orbitally tuned Perales section periodic and transient reductions of PF abundance before the MSC occur in levels corresponding to eccentricity minima (Sierro et al., 2003). It is worth noting that despite the FR can be found at slightly different ages, the FD, recognized by planktic (PFD), benthic (BFD) or indistinct assemblages (FD), is always found in the same precessional cycle (Fig. 11; Manzi et al., 2018, 2021). Thus, we suggest that the early FR heralds the lack of primary gypsum sedimentation in relatively deep and poorly oxygenated setting (Manzi et al., 2021 and references therein) of the Eastern and Central Mediterranean driven by local paleoenvironmental factors, whereas the FD at the MSC onset depends by a synchronous change at the Mediterranean scale.

5.3.2.2. Calcareous nannofossils. CN do not record the early decline in abundance showed by foraminifera, but only a decrease of diversity. The resilience of CN compared to the PF before and across the MSC onset was observed in other successions (Manzi et al., 2021; Mancini et al., 2022) and explained with their adaptability to a wider range of environments and their minor susceptibility to dissolution. Opposite to PF, CN can thrive in the modern low salinity Black Sea (Kubryakov et al., 2019; Kubryakov et al., 2021) and in the high salinity Red Sea during the Last Glacial Maximum (Lars-Legge et al., 2008). These adaptations favor CN in the increasingly variable environment reconstructed after 6.2 Ma in the UMs.

Other than its resilience as a group, the decrease of CN diversity results in a succession of almost monospecific acme/peaks starting from that of the *R. antartica/perplexa* (6.058–6.018 Ma in the UMs) and ending with the MSC onset bioevent (Lozar and Negri, 2019; Mancini et al., 2020). The acme of *R. antartica/perplexa* is, at present, only recorded in the Eastern Mediterranean (UMs and Tokhni section), whereas just a short influx is recorded in the Western Mediterranean at the end of the acme (cycle UA32 of the Perales section, ca. 6.02 Ma; Mancini et al., 2020). *R. antartica/perplexa* is an extinct taxon, abundant at high latitude in the Southern Ocean during the Miocene, where its relative increase respect to *C. pelagicus* is used to reconstruct surface water cooling phases (Wei and Wise, 1992). In addition, *R. antartica/perplexa* was documented in Eastern Europe Oligocene marine sediments influenced by freshwater input (Krhovský et al., 1992). An overall cooler climate, as predicted by the prominent marine isotopic stage 2 and the associated relatively cold interglacials (Van der Laan et al., 2005), and the greater influx of continental waters could have favored the proliferation of this CN taxon in an interval also characterized by enhanced water exchange between the Mediterranean and the Paratethys (Stoica et al., 2013). Interestingly, these conditions were more typical of the Eastern Mediterranean, where they lasted for longer time than in the Western Mediterranean.

After the *R. antartica/perplexa* acme, the peaks of *Sphenolitus* spp., *H. carteri* and *U. rotula*, compose the CN MSC bioevent after the second hydrological step, when also insolation minima have $^{87}Sr/^{86}Sr$ signature lower than the global Ocean. This bioevent is documented in a suite of outcropping successions (Lozar and Negri, 2019), and a similar opportunistic CN assemblage was also documented in cutting samples of the Dolphin well in the Levantine Basin (Manzi et al., 2021). The succession of these peaks is interpreted by Mancini et al. (2020) as the response of CN to the final 6.0 Ma tectonic restriction of the Mediterranean, that became more and more sensitive to surface water nutrient enrichment from runoff. Mancini et al. (2022) and Manzi et al. (2021) also showed that opportunistic CN assemblages are recorded in the PLG unit, both in the relatively shallow Sorbas Basin and in the deeper Levantine Basin, respectively.

5.3.3. The origin of the carbonate precipitation at 6.0 Ma and the salinity scenario at the MSC onset

The revised age model of the UMs, retained in our work, and the evaporitic origin of the first prominent limestone based on the mm-scale lamination of the lime mud, here referred to as laminated grainstone A (Fig. 2B), has led Zachariasse and Lourens (2021) to infer an earlier onset of the MSC in the Eastern Mediterranean (6.00 Ma). The same interpretation was extended to the first limestone bed (upper part of cycle 49) of the Falconara section (Sicily) that, according to Hilgen and Krijgsman (1999), should mark the MSC onset. Despite both described as carbonate beds, the Falconara one differs from that of the UMs by having a dolomitic composition and heavier $\delta^{18}O$ (6–7 ‰); these aspects have not been considered by Zachariasse and Lourens (2021). In fact, the $\delta^{18}O$ and $\delta^{13}C$ measured on the 6.00 Ma bed A of the UMs are slightly negative, excluding its evaporitic origin. Moreover, the rare presence of evaporitic minerals a few millimeters across, consisting of calcite pseudomorphs after gypsum, suggests that conditions for gypsum precipitation only occurred locally and were quickly disrupted by dilution with evaporite minerals dissolution and replacement.

The claimed evaporitic 6.00 Ma episode in the Eastern Mediterranean represents the culmination of a high salinity pre-evaporitic scenario starting from the earliest Messinian, as reconstructed by different authors (Zachariasse and Lourens, 2021; Butiseacă et al., 2022; Kontakiotis et al., 2022), which is at odd with the increasing restriction and continental water influence reconstructed by means of geochemistry, micropaleontology and petrography for the UMs.

To reconcile this contradiction, we suggest that the high salinity phase was a prerogative of the Eastern Mediterranean only during the early pre-evaporitic phase (up to 6.4 Ma). This phase led to the formation and accumulation of progressively denser deep waters. Accordingly, the denser deep waters were progressively more difficult to renew, slowing down the main process of thermohaline circulation in the Eastern Mediterranean (Rohling et al., 2015) and, hence, the water exchange with the Western Mediterranean and the Atlantic.

With low proportion of Atlantic waters entering the Mediterranean, any successive runoff pulse at insolation maxima was increasingly able to deviate the characteristics of surface waters, as reflected by the $^{87}Sr/^{86}Sr$ excursions below global oceanic values (Reghizzi et al., 2017 and this work), lighter $\delta^{18}O$ and $\delta^{13}C$ of PF (Zachariasse and Lourens, 2021) and decreasing sea surface salinity after 6.2 Ma (Vasiliev et al., 2019). In such variable environment, the surface water conditions selected those opportunistic taxa able to withstand nutrient and salinity variations in warm waters (*O. universa*; Brachert et al., 2015; Marshall et al., 2015), salinity variation in cold and eutrophic waters (turborotalids; Kroon et al., 1988) and water column stratification (*S. abies* and neogloboquadrinids; Mancini et al., 2020; Schiebel and Hemleben, 2017). The early deterioration of the foraminifer habitat (FR) probably reflected the susceptibility of this group to environmental variability associated to the step-by-step progression towards the crisis. Contrary to foraminifera, CN are more adaptable to salinity fluctuations (Kubryakov et al., 2019; Legge et al., 2008) and reacted by increasing the dominance of few species, such as *R. perplexa*, *S. abies*, *H. carteri* and *U. jafari* (see also Lozar and Negri, 2019). The CN biovent at the MSC onset, clearly related in time in both deep and shelf successions, suggests that the final step before gypsum deposition in marginal settings involved a Mediterranean-scale synchronous environmental change explained with increasing restriction and continental influence (Mancini et al., 2020).

6. Conclusions

Our integrated stratigraphic analysis of the Upper Metochia section on the Gavdos Island confirms the cyclostratigraphic revision after Krijgsman et al. (2004) provided by Zachariasse and Lourens (2021) indicating an age of 6.0 Ma for the first limestone bed (their bed M130, our limestone A) in the upper part of the section. However, the negative $\delta^{18}O$ and the absence of widespread evaporite minerals, characterizing

bed lgA of the UMs, suggest that no clear and/or permanent evaporitic conditions occurred at that time; thus, ruling out the hypothesis of an earlier onset of the salinity crisis in the Eastern Mediterranean. The MSC onset is instead best predated (the influx *B. bigelowi* at ca. 6.168 Ma and acme of *R. perplexa* at ca. 6.058–6.018 Ma) and approximated (peaks of *Sphenolitus* spp. and *H. carteri* at ca. 5.990 and 5.973 Ma, respectively) by astronomically calibrated calcareous nannofossil biostratigraphic events.

We also provide new insights on the paleoceanographic evolution of the Eastern Mediterranean approaching the MSC. Variability of $^{87}Sr/^{86}Sr$ suggest that surface Mediterranean waters were increasingly influenced by continental inflows from 6.2 Ma, especially at insolation maxima. The consequent restriction caused local to regional differences in the paleoenvironmental response to the orbital configuration. Conversely, normal oceanic connection persisted at insolation minima up to 5.96 Ma, when homogeneous paleoceanographic conditions were established across the Mediterranean. The increasing runoff influence led to enhanced salinity oscillations and overall nutrient availability. This environmental pressure affected foraminifera and CN, that decreased diversity and selected taxa with eutrophic affinity and a broad salinity tolerance. Foraminifera were more severely affected and, other than a diversity decrease, they first underwent a reduction in abundance (FR; 6.068 Ma) only in open marine settings and finally disappeared (FD 5.97 Ma), in both marginal and open settings. CN were more resilient and produced peaks of almost monospecific assemblages before the final decline at the 5.97 Ma.

Supplementary data to this article can be found online at https://doi.org/10.1016/j.palaeo.2023.111970.

CRediT authorship contribution statement

Rocco Gennari: Conceptualization, Data curation, Formal analysis, Investigation, Methodology, Supervision, Validation, Visualization, Writing – original draft, Writing – review & editing. **Stefano Lugli:** Conceptualization, Formal analysis, Methodology, Supervision, Validation, Writing – review & editing. **Vinicio Manzi:** Conceptualization, Funding acquisition, Investigation, Methodology, Supervision, Validation, Visualization, Writing – review & editing. **Davide Persico:** Data curation, Formal analysis, Validation. **Matteo Reghizzi:** Data curation, Formal analysis. **Marco Roveri:** Conceptualization, Funding acquisition, Investigation, Resources, Supervision, Validation, Writing – review & editing.

Declaration of Competing Interest

The authors declare that they have no known competing financial interests or personal relationships that could have appeared to influence the work reported in this paper.

Data availability

Data will be made available on request.

Acknowledgments

This research has been cofinanced by the European Union (European Social Fund – ESF) and Greek National Funds through the Operational Program 'Education and Life- long Learning' of the National Strategic Reference Framework (NSRF) - Research Funding Program: THA-LIS-UOA-'Messinian Salinity Crisis: the greatest Mediterranean environmental perturbation and its repercussions to the biota'. This research was also funded by a MIUR (Ministero dell'Istruzione, dell'Università e della Ricerca, Italy) grant to M. Roveri (PRIN 2008). Vasileios Karakitsios is warmly thanked for the logistic and field support.

References

Aksu, A.E., Hiscott, R.N., Kaminski, M.A., Mudie, P.J., Gillespie, H., Abrajano, T., Yasar, D., 2002. Last glacial – Holocene paleoceanography of the Black Sea and Marmara Sea: stable isotopic, foraminiferal and coccolith evidence. Mar. Geol. 190, 119–149.

Bellanca, A., Caruso, A., Ferruzza, G., Neri, R., Rouchy, J.M., Sprovieri, M., 2001. Transition from marine to hypersaline conditions in the Messinian Tripoli Formation from the marginal areas of the central Sicilian Basin. Sediment. Geol. 140, 87–105.

Blanc-Valleron, M.M., Pierre, C., Caulet, J.P., Caruso, A., Rouchy, J.M., Cespuglio, G., Sprovieri, R., Pestrea, S., Di Stefano, E., 2002. Sedimentary, stable isotope and micropaleontological records of paleoceanographic change in the Messinian Tripoli Formation (Sicily, Italy). Palaeogeogr. Palaeoclimatol. Palaeoecol. 185, 255–286.

Bosmans, J.H.C., Drijfhout, S.S., Tuenter, E., Hilgen, F.J., Lourens, L.J., Rohling, E.J., 2015. Precession and obliquity forcing of the freshwater budget over the Mediterranean. Quat. Sci. Rev. 123, 16–30. ISSN 0277-3791,. https://doi.org/10.1016/j.quascirev.2015.06.008.

Bown, P.R., Young, J.R., 1998. Techniques. In: Bown, P.R. (Ed.), Calcareous Nannofossil Biostratigraphy. Kluwer Academic Publications, Dordrecht, Netherlands, pp. 16–28.

Brachert, T., Bornemann, A., Reuter, M., Galer, S., Grimm, K., Fassoulas, C., 2015. Upwelling history of the Mediterranean Sea revealed by stunted growth in the planktic foraminifera *Orbulina universa* (early Messinian, Crete, Greece). Int. J. Earth Sci. 104 (1), 263–276.

Bulian, F., Kouwenhoven, T.J., Jiménez-Espejo, F.J., Krijgsman, W., Andersen, N., Sierro, F.J., 2022. Impact of the Mediterranean-Atlantic connectivity and the late Miocene car- bon shift on deep-sea communities in the Western Alboran Basin. Palaeogeogr. Palaeoclimatol. Palaeoecol. 589, 110841 https://doi.org/10.1016/j.palaeo.2022.110841.

Butiseacă, G.A., van der Meer, M.T.J., Kontakiotis, G., Agiadi, K., Thivaiou, D., Besiou, Antonarakou A., Mulch, A., Vasiliev, I., 2022. Multiple crises preceded the Mediterranean Salinity Crisis: Aridification and vegetation changes revealed by biomarkers and stable isotopes. Glob. Planet. Chang. 217, 103951.

Capella, W., Barhoun, N., Flecker, R., Hilgen, F.J., Kouwenhoven, T.J., Matenco, L., Sierro, F.J., Tulbure, M.A., Yousfi, M.Z., Krijgsman, W., 2018. Palaeogeographic evolution of the late Miocene Rifian Corridor (Morocco): Reconstructions from surface and subsurface data. Earth Sci. Rev. 180, 37–59. https://doi.org/10.1016/j.earscirev.2018.02.017.

Capella, W., Flecker, R., Hernàndez-Molina, F.J., Simon, D., Meijer, P.T., Rogerson, M., Sierro, F.J., Krijgsman, W., 2019. Mediterranean isolation preconditioning the Earth System for late Miocene climate cooling. Sci. Rep. 9 (1), 1–8. https://doi.org/10.1038/s41598-019-40208-2.

Corbí, H., Soria, J.M., Giannetti, A., Yébenes, A., 2020. The step-by-step restriction of the Mediterranean (start, amplification, and consolidation phases) preceding the Messinian Salinity Crisis (climax phase) in the Bajo Segura basin. Geo-Mar. Lett. 1–21 https://doi.org/10.1007/s00367-020-00647-7.

Darling, K.F., Wade, C.M., 2008. The genetic diversity of planktic foraminifera and the global distribution of ribosomal RNA genotypes. Mar. Micropaleontol. 67, 216–238. https://doi.org/10.1016/j.marmicro.2008.01.009.

Dela Pierre, F., Bernardi, E., Cavagna, S., Clari, P., Gennari, R., Irace, A., Lozar, F., Lugli, S., Manzi, V., Natalicchio, M., Roveri, M., Violanti, D., 2011. The record of the Messinian salinity crisis in the Tertiary Piedmont Basin (NW Italy): the Alba section revisited. Paleogeogr. Paleoclimatol. Paleoecol. 310, 238–255. https://doi.org/10.1016/j.paleo.2011.07.017.

Drinia, H., Antonarakou, A., Tsaparas, N., Kontakiotis, G., 2007. Palaeoenvironmental conditions preceding the Messinian Salinity Crisis: a case study from Gavdos Island. Geobios 40, 251–265.

Duggen, S., Hoernle, K., van den Bogaard, P., Rüpke, L., Phipps-Morgan, J., 2003. Deep roots of the Messinian salinity crisis. Nature 422, 602–606.

Filippelli, G.M., Flores, J.A., Vázquez, R., Utrilla, R., Pérez-Folgado, M., Latimer, C., 2003. A sediment-nutrient-oxygen feedback responsible for productivity variations in late Miocene sapropel sequences of the western Mediterranean. Palaeogeogr. Palaeoclimatol. Palaeoecol. 190, 335–348.

Flecker, R., Ellam, R.M., 2006. Identifying Late Miocene episodes of connection and isolation in the Mediterranean–Paratethyan realm using Sr isotopes. Sediment. Geol. 188–189, 189–203.

Flores, J.A., Sierro, F.J., Filippelli, G.M., Barcena, M.A., Pérez-Folgado, M., Vazquez, A., Utrilla, R., 2005. Surface water dynamics and phytoplankton communities during deposition of cyclic late Messinian sapropel sequences in the western Mediterranean. Mar. Micropaleontol. 56, 50–79.

Garcia-Castellanos, D., Villaseñor, A., 2011. Messinian salinity crisis regulated by competing tectonics and erosion at the Gibraltar arc. Nature 480, 359–363.

Gennari, R., Manzi, V., Angeletti, L., Bertini, A., Biffi, U., Ceregato, A., Faranda, C., Gliozzi, E., Lugli, S., Menichetti, E., Rosso, A., Roveri, M., Taviani, M., 2013. A shallow water record of the onset of the Messinian salinity crisis in the Adriatic foredeep (Legnagnone section, Northern Apennines). Palaeogeogr. Palaeoclimatol. Palaeoecol. 386, 145–164.

Gennari, R., Lozar, F., Turco, E., Dela Pierre, F., Lugli, S., Manzi, V., Natalicchio, M., Roveri, M., Schreiber, B.C., Taviani, M., 2018. Integrated stratigraphy and paleoceanographic evolution of the pre-evaporitic phase of the Messinian salinity crisis in the Eastern Mediterranean as recorded in the Tokhni section (Cyprus island). Newsl. Stratigr. 51, 33–55. https://doi.org/10.1127/nos/2017/0350.

Gennari, R., Lozar, F., Natalicchio, M., Zanella, E., Carnevale, G., Dela Pierre, F., 2020. Chronology of the Messinian events in the northernmost part of the Mediterranean: the Govone section (Piedmont Basin, NW Italy). Riv. Ital. Paleontol. Stratigr. 126, 517–560.

Gladstone, R., Flecker, R., Valdes, P., Lunt, D., Markwick, P., 2007. The Mediterranean hydrologic budget from a late Miocene global climate simulation. Palaeogeogr. Palaeoclimatol. Palaeoecol. 251, 254–267.
Griffin, D.L., 2002. Aridity and humidity: two aspects of the late Miocene climate of North Africa and the Mediterranean. Palaeogeogr. Palaeoclimatol. Palaeoecol. 182, 65–91.
Griffin, D.L., 2006. The late Neogene Sahabi rivers of the Sahara and their climatic and environmental implications for the Chad Basin. J. Geol. Soc. Lond. 163, 905–921.
Grothe, A., Andreetto, F., Reichart, G.J., Wolthers, M., Van Baak, C.G., Vasiliev, I., Stoica, M., Sangiorgi, F., Middelburg, J.J., Davies, G.R., Krijgsman, W., 2020. Paratethys pacing of the Messinian Salinity Crisis: low salinity waters contributing to gypsum precipitation? Earth Planet. Sci. Lett. 532, 116029 https://doi.org/10.1016/j.epsl.2019.116029.
Hilgen, F.J., Krijgsman, W., 1999. Cyclostratigraphy and astrochronology of the Tripoli diatomite formation (pre-evaporite Messinian, Sicily, Italy). Terra Nova 11, 16–22.
Hilgen, F.J., Krijgsman, W., Langereis, C.G., Lourens, L.J., Santarelli, A., Zachariasse, W. J., 1995. Extending the astronomical (polarity) time scale into the Miocene. Earth Planet. Sci. Lett. 136, 495–510.
Holbourn, A.E., Kuhnt, W., Clemens, S.C., Kochhann, K.G.D., Jöhnck, J., Lübbers, J., Andersen, N., 2018. Late Miocene climate cooling and intensification of southeast Asian winter monsoon. Nat. Commun. 9, 1584. https://doi.org/10.1038/s41467-018-03950-1.
Hüsing, S.K., Kuiper, K.F., Link, W., Hilgen, F.J., Krijgsman, W., 2009. The upper Tortonian–lower Messinian at Monte Dei Corvi (Northern Apennines, Italy): Completing a Mediterranean reference section for the Tortonian Stage. Earth Planet. Sci. Lett. 282 (1–4), 140–157. https://doi.org/10.1016/j.epsl.2009.03.010.
Hüsing, S.K., Oms, O., Agustí, J., Garcés, M., Kouwenhoven, T.J., Krijgsman, W., Zachariasse, W.-J., 2012. On the late Miocene continentalization of the Guadix Basin: more evidence for a major Messinian hiatus. Geobios 45, 617–620.
Ijiri, A., Wang, L., Oba, T., Kawahata, H., Huang, C.-Y., Huang, C.-Y., 2005. Paleoenvironmental changes in the northern area of the East China Sea during the past 42,000 years. Palaeogeogr. Palaeoclimatol. Palaeoecol. 219, 239–261.
Karakitsios, V., Roveri, M., Lugli, S., Manzi, V., Gennari, G., Antonarakou, A., Triantaphyllou, M., Agiadi, K., Kontakiotis, G., Kafousia, N., de Rafelis, M., 2017. A record of the Messinian salinity crisis in the eastern Ionian tectonically active domain (Greece, eastern Mediterranean). Basin Res. 29, 203–233. https://doi.org/10.1111/bre.12173.
Kontakiotis, G., Butiseacă, G.-A., Karakitsios, V., Antonarakou, A., Zarkogiannis, S., Agiadi, K., Krsnik, E., Besiou, E., Zachariasse, J.-W., Lourens, L., Thivaiou, D., Koskeridou, E., Moissette, P., Mulch, A., Vasiliev, I., 2022. Hypersalinity accompanies tectonic restriction in the eastern Mediterranean prior to the Messinian Salinity Crisis. Palaeogeogr. Palaeoclimatol. Palaeoecol. 592 (2), 110903 https://doi.org/10.1016/j.palaeo.2022.110903.
Kouwenhoven, T.J., Hilgen, F.J., van der Zwaan, G.J., 2003. Late Tortonian–early Messinian stepwise disruption of the Mediterranean–Atlantic connections: constraints from benthic foraminiferal and geochemical data. Palaeogeogr. Palaeoclimatol. Palaeoecol. 18, 303–319.
Kouwenhoven, T.J., Morigi, C., Negri, A., Giunta, S., Krijgsman, W., Rouchy, J.M., 2006. Paleoenvironmental evolution of the eastern Mediterranean during the Messinian: Constraints from integrated microfossil data of the Pissouri Basin (Cyprus). Mar. Micropaleontol. 60, 17–44. https://doi.org/10.1016/j.marmicro.2006.02.005.
Krhovský, J., Adamová, J., Hladíková, J., Maslowská, H., 1992. Paleoenviromental changes across the Eocene/Oligocene boundary in the Ždánice and Pouzdřany units (Western Carpathians, Czechoslovakia): the long-term trend and orbitally forced changes in calcareous nannofossil assemblages. In: Hamršmid, B., Young, J. (Eds.), Nannoplankton research II. Proceedings of 4th INA Conference, Prague, 1991. Knihovnička Zemního Plynu a Nafty, 14b, 2, pp. 105–187.
Krijgsman, W., Hilgen, F.J., Raffi, I., Sierro, F.J., Wilson, D.S., 1999. Chronology, causes, and progression of the Messinian salinity crisis. Nature 400, 652–655.
Krijgsman, W., Gaboardi, S., Hilgen, F.J., Iaccarino, S., de Kaenel, E., van der Laan, E., 2004. Revised astrochronology for the Ain el Beida section (Atlantic Morocco): no glacio-eustatic control for the onset of the Messinian Salinity Crisis. Stratigraphy 1, 87–101.
Krijgsman, W., Capella, W., Simon, D., Hilgen, F.J., Kouwenhoven, T.J., Meijer, P.Th., Sierro, F.J., Tulbure, M.A., van den Berg, B.C.J., van der Schee, M., Flecker, R., 2018. The Gibraltar Corridor: watergate of the Messinian salinity crisis. Mar. Geol. 403, 238–246. https://doi.org/10.1016/j.margeo.2018.06.008.
Kroon, D., Wouters, P., Moodley, L., Ganssen, G., Troelstra, S.R., 1988. Phenotypic variation of Turborotalita quinqueloba (Natland) tests in living populations and in the Pleistocene of an eastern Mediterranean piston core. In: Brummer, G.J.A., Kroon, D. (Eds.), Planktonic Foraminifers as Tracers of Ocean-Climate History. Free Univ. Press, Amsterdam, pp. 131–143.
Kubryakov, A.A., Mikaelyan, A.S., Stanichny, S.V., 2019. Summer and winter coccolithophore blooms in the Black Sea and their impact on production of dissolved organic matter from Bio-Argo data. J. Mar. Syst. 199, 103220 https://doi.org/10.1016/j.jmarsys.2019.103220.
Kubryakov, A.A., Mikaelyan, A.S., Stanichny, S.V., 2021. Extremely strong coccolithophore blooms in the Black Sea: the decisive role of winter vertical entrainment of deep water. Deep-Sea Res. I Oceanogr. Res. Pap. 173, 103554.
Laskar, J., Robutel, P., Joutel, F., Gastineau, M., Correia, A.C.M., Levrard, B., 2004. A long-term numerical solution for the insolation quantities of the Earth. Astron. Astrophys. 428, 261–285. https://doi.org/10.1051/0004-6361:20041335.
Legge, H.L., Mutterlose, J., Arz, H.W., Pätzold, J., 2008. Nannoplankton successions in the northern Red Sea during the last glaciation (60 to 14.5 ka BP): Reactions to climate change. Earth Planet. Sci. Lett. 270 (3–4), 271–279. https://doi.org/10.1016/j.epsl.2008.03.030.
Lirer, F., Foresi, L.M., Iaccarino, S.M., Salvatorini, G., Turco, E., Cosentino, C., Sierro, F. J., Caruso, A., 2019. Mediterranean Neogene planktonic foraminifer biozonation and biochronology. Earth Sci. Rev. 196, 102869.
Lozar, F., Negri, A., 2019. A review of basin-wide calcareous nannofossil bioevents in the Mediterranean at the onset of the Messinian salinity crisis. Mar. Micropaleontol. 151, 101752.
Mancini, A.M., Gennari, R., Ziveri, P., Mortyn, P.G., Stolwijk, D.J., Lozar, F., 2020. Calcareous nannofossil and foraminiferal trace element records in the Sorbas Basin: a new piece of the Messinian Salinity Crisis onset puzzle. Palaeogeogr. Palaeoclimatol. Palaeoecol. 554. https://doi.org/10.1016/j.palaeo.2020.109796.
Lozar, F., Violanti, D., Bernardi, E., Dela Pierre, F., Natalicchio, M., 2018. Identifying the onset of the Messinian salinity crisis: a reassessment of the biochronostratigraphic tools (Piedmont Basin, NW Italy). Newslett. Stratigr. 51 (1), 11–31.
Mancini, A.M., Gennari, R., Natalicchio, M., Pierre, F.D., Carnevale, G., Pastero, L., Pellegrino, L., Pilade, F., Lozar, F., 2022. Taphonomic bias on calcareous micro and nannofossils and paleoenvironmental evolution across the Messinian Salinity Crisis onset: insights from the Sorbas Basin (SE Spain). Palaeogeogr. Palaeoclimatol. Palaeoecol. 599, 111056 https://doi.org/10.1016/j.palaeo.2022.111056.
Mansour, B., Bessedik, M., Saint Martin, J.P., Belkebir, L., 2008. Signification paléoécologique des assemblages de diatomées du Messinien du Dahra sud-occidental (bassin du Chélif, Algérie nord-occidentale). Geodiversitas 30 (1), 117–139.
Manzi, V., Roveri, M., Gennari, R., Bertini, A., Biffi, U., Giunta, S., Iaccarino, S.M., Lanci, L., Lugli, S., Negri, A., Riva, A., Rossi, M.E., Taviani, M., 2007. The deep-water counterpart of the Messinian lower Evaporites in the Apennine foredeep: the Fanantello section (Northern Apennines, Italy). Palaeogeogr. Palaeoclimatol. Palaeoecol. 251, 470–499.
Manzi, V., Lugli, S., Roveri, M., Schreiber, B.C., Gennari, R., 2011. The Messinian "Calcare di Base" (Sicily, Italy) revisited. Geol. Soc. Am. Bull. 123, 347–370.
Manzi, V., Gennari, R., Hilgen, F., Krijgsman, W., Lugli, S., Roveri, M., Sierro, F.J., 2013. Age refinement of the Messinian salinity crisis onset in the Mediterranean. Terra Nova 25, 315–322.
Manzi, V., Lugli, S., Roveri, M., Dela Pierre, F., Gennari, R., Lozar, F., Natalicchio, M., Schreiber, B.C., Taviani, M., Turco, E., 2016. The Messinian salinity crisis in Cyprus: a further step toward a new stratigraphic framework for Eastern Mediterranean. Basin Res. 28, 207–236.
Manzi, V., Gennari, R., Lugli, S., Persico, D., Reghizzi, M., Roveri, M., Schreiber, B.C., Calvo, R., Gavrieli, I., Gvirtzman, Z., 2018. The onset of the Messinian salinity crisis in the deep Eastern Mediterranean basin. Terra Nova 30 (3), 189–198. https://doi.org/10.1111/ter.12325.
Manzi, V., Gennari, R., Lugli, S., Persico, D., Roveri, M., Gavrieli, I., Gvirtzman, Z., 2021. Synchronous onset of the Messinian salinity crisis and diachronous evaporite deposition: New evidences from the deep Eastern Mediterranean basin. Palaeogeogr. Palaeoclimatol. Palaeoecol. 584, 110685 https://doi.org/10.1016/j.palaeo.2021.110685.
Marshall, B.J., Thunell, R.C., Spero, H.J., Henehan, M.J., Lorenzoni, L., Astor, Y., 2015. Morphometric and stable isotopic differentiation of Orbulina universa morphotypes from the Cariaco Basin, Venezuela. Mar. Micropaleontol. 120, 46–64.
Marzocchi, A., Lunt, D., Flecker, R., Bradshaw, C., Farnsworth, A., Hilgen, F., 2015. Orbital control on late Miocene climate and the North African monsoon: insight from an ensemble of sub-precessional simulations. Clim. Past 11 (10), 1271–1295.
McArthur, J.M., Howarth, R.J., Bailey, T.R., 2001. Strontium isotope stratigraphy: LOWESS version 3: best fit to the marine Sr-isotope curve for 0–509 Ma and accompanying look-up table for deriving numerical age. J. Geol. 109, 155–170.
McArthur, J.M., Howarth, R.J., Shields, G.A., 2012. Strontium isotope stratigraphy. In: Gradstein, F.M., Ogg, J.G., Schmitz, M.D., Ogg, G.M. (Eds.), The Geological Time Scale 2012. Elsevier B.V, Oxford, pp. 127–144.
Melki, T., Kallel, N., Fontugne, M., 2010. The nature of transitions from dry to wet condition during sapropel events in the Eastern Mediterranean Sea. Palaeogeogr. Palaeoclimatol. Palaeoecol. 291 (3–4), 267–285.
Miller, K.G., Mountain, G.S., Wright, J.D., Browning, J.V., 2011. A 180-million-year record of sea level and ice volume variations from continental margin and deep-sea isotopic records. Oceanography 24 (2), 40–53. https://doi.org/10.5670/oceanog.2011.26.
Modestou, S., Simon, D., Gutjahr, M., Marzocchi, A., Kowenhoven, T.J., Ellam, R.M., Flecker, R., 2017. Precessional variability of $^{87}Sr/^{86}Sr$ in the late Miocene Sorbas Basin: an interdisciplinary study of drivers of interbasin exchange. Paleoceanography 32, 1–22.
Morard, R., Quillévéré, F., Escarguel, G., Ujiie, Y., de Garidel-Thoron, T., Norris, R.D., de Vargas, C., 2009. Morphological recognition of cryptic species in the planktonic foraminifer *Orbulina universa*. Mar. Micropaleontol. 71, 148–165.
Ng, Z.L., Hernández-Molina, F.J., Duarte, D., Sierro, F.J., Ledesma, S., Rogerson, M., Llave, E., Roque, C., Manar, M.A., 2021. Latest Miocene restriction of the Mediterranean Outflow Water: a perspective from the Gulf of Cádiz. Geo-Mar. Lett. 41, 23. https://doi.org/10.1007/s00367-021-00693-9.
Orszag-Sperber, F., 2006. Changing perspectives in the concept of "Lago-Mare" in Mediterranean late Miocene evolution. Sediment. Geol. 188, 259–277.
Pellegrino, L., Dela, Pierre F., Natalicchio, M., Carnevale, G., 2018. The Messinian diatomite deposition in the Mediterranean and its relationships to the global silica cycle. Earth Sci. Rev. 178, 154–176.
Perez-Folgado, M., Sierro, F.J., Barcena, M.A., Flores, J.A., Vazquez, A., Utrilla, R., Hilgen, F.J., Krijgsman, W., Filippelli, G.M., 2003. Western versus eastern Mediterranean paleoceanographic response to astronomical forcing: a high-resolution microplankton study of precession-controlled sedimentary cycles during the Messinian. Palaeogeogr. Palaeoclimatol. Palaeoecol. 190, 317–334.

Pestrea, S., Blanc-Valleron, M.M., Rouchy, J.M., 2002. Les assemblages de diatomées des niveaux infra-gypseux du Messinien de Méditerranée (Espagne, Sicile, Chypre). Geodiversitas 24 (3), 543–583.
Reghizzi, M., Gennari, R., Douville, E., Lugli, S., Manzi, V., Montagna, P., Roveri, M., Sierro, F.J., Taviani, M., 2017. Isotope stratigraphy ($^{87}Sr/^{86}Sr$, $\delta^{18}O$, $\delta^{13}C$) of the Sorbas basin (Betic Cordillera, Spain): paleoceanographic evolution across the onset of the Messinian salinity crisis. Palaeogeogr. Palaeoclimatol. Palaeoecol. 469, 60–73.
Reghizzi, M., Lugli, S., Manzi, V., Rossi, F.P., Roveri, M., 2018. Orbitally forced hydrological balance during the Messinian salinity crisis: insights from strontium isotopes ($^{87}Sr/^{86}Sr$) in the Vena del Gesso basin (Northern Apennines, Italy). Palaeogeogr. Palaeoclimatol. Palaeoecol. 33, 716–731.
Riforgiato, F., Foresi, L.M., Aldinucci, M., Mazzei, R., Donia, F., Gennari, R., Salvatorini, G., Sandrelli, F., 2008. Foraminiferal record and astronomical cycles: an example from the Messinian pre-evaporitic Gello Composite Section (Tuscany, Italy). Stratigraphy 2008 (5), 265–280.
Roveri, M., Lugli, S., Manzi, V., Schreiber, B.C., 2008. The Messinian Sicilian stratigraphy revisited: toward a new scenario for the Messinian salinity crisis. Terra Nova 20, 483–488.
Rohling, E.J., Marino, G., Grant, K.M., 2015. Mediterranean climate and oceanography, and the periodic development of anoxic events (sapropels). Earth-Sci. Rev. 143, 62–97.
Roveri, M., Flecker, R., Krijgsman, W., Lofi, J., Lugli, S., Manzi, V., Sierro, F., Bertini, A., Camerlenghi, A., De Lange, G., Govers, R., Hilgen, F., Hübscher, C., Meijer, P.T., Stoica, M., 2014a. The Messinian salinity crisis: past and future of a great challenge for marine sciences. Mar. Geol. 352, 25–58.
Roveri, M., Lugli, S., Manzi, V., Gennari, R., Schreiber, B.C., 2014b. High-resolution strontium isotope stratigraphy of the Messinian deep Mediterranean basins: implications for marginal to central basin correlation. Mar. Geol. 349, 113–125.
Roveri, M., Lugli, S., Manzi, V., Reghizzi, M., Rossi, F.P., 2020. Stratigraphic relationships between shallow-water carbonates and primary gypsum: insights from the Messinian succession of the Sorbas Basin (Betic Cordillera, Southern Spain). Sediment. Geol. 404, 105678.
Saint Martin, S., Conesa, G., Saint Martin, J.P., 2003. Les assemblages de diatomées du Messinien dans le basin de Melilla-Nador (Rif Nord-Oriental Maroc). Rev. Micropaleontol. 46, 161–190. https://doi.org/10.1016/j.revmic.2007.02.004.
Schiebel, R., Hemleben, C., 2017. Planktic Foraminifer in the Modern Ocean. Springer-Verlag, Berlin, Heidelberg, 358 pp.
Schimmelmann, A., Lange, B., C, B., Schieber, J., Francus, P., Ojala, A.E.K., Zolitschk, B., 2016. Varves in marine sediments: a review. Earth Sci. Rev. 159, 215–246.
Schumacher, S., Jorissen, F.J., Dissard, D., Larkin, K.E., Gooday, A.J., 2007. Live (Rose Bengal stained) and dead benthic foraminifera from the oxygen minimum zone of the Pakistan continental margin (Arabian Sea). Mar. Micropaleontol. 62, 45–73.
Seidenkrantz, M.-S., Kouwenhoven, T.J., Jorissen, F.J., Shackleton, N.J., van der Zwaan, G.J., 2000. Benthic foraminifera as indicators of changing Mediterranean–Atlantic water exchange in the late Miocene. Mar. Geol. 163, 387–407.
Sierro, F.J., Krijgsman, W., Hilgen, F.J., Flores, J.A., 2001. The Abad composite (SE Spain): a Mediterranean reference section for the Messinian and the Astronomical Polarity Time Scale (APTS). Palaeogeogr. Palaeoclimatol. Palaeoecol. 168, 143–172.
Sierro, F.J., Flores, J.A., Francés, G., Vazquez, A., Utrilla, R., Zamarreño, I., Erlenkeuser, H., Barcena, M.A., 2003. Orbitally controlled oscillations in planktic communities and cy- clic changes in western Mediterranean hydrography during the Messinian. Palaeogeogr. Palaeoclimatol. Palaeoecol. 190, 289–316.
Simon, D., Meijer, P., 2015. Dimensions of the Atlantic–Mediterranean connection that caused the Messinian Salinity Crisis. Mar. Geol. 364, 53–64.
Simon, D., Meijer, P.T., 2017. Salinity stratification of the Mediterranean Sea during the Messinian crisis: a first model analysis. Earth Planet. Sci. Lett. 479, 366–376.
Simon, D., Marzocchi, A., Flecker, R., Lunt, D.J., Hilgen, F.J., Meijer, P.T., 2017. Quantifying the Mediterranean freshwater budget throughout the late Miocene: New implications for sapropel formation and the Messinian Salinity Crisis. Earth Planet. Sci. Lett. 472, 25–37.
Stoica, M., Lazăr, I., Krijgsman, W., Vasiliev, I., Jipa, D., Floroiu, A., 2013. Paleoenvironmental evolution of the East Carpathian foredeep during the late Miocene–early Pliocene (Dacian Basin; Romania). Glob. Planet. Chang. 103, 135–148.
Tuenter, E., Weber, S.L., Hilgen, F.J., Lourens, L.J., 2003. The response of the African summer monsoon to remote and local forcing due to precession and obliquity. Glob. Planet. Chang. 36, 219–235. https://doi.org/10.1016/S0921-8181(02)00196-0.
Tzevahirtzian, A., Caruso, A., Andreetto, F., Bonomo, S., Krijgsman, W., 2023. A biochronostratigraphic study of the upper Miocene from the northern Caltanissetta Basin, Sicily (core 3AGN2S04). Implications for dating the Messinian Salinity Crisis onset. Sediment. Geol. 445, 106330.
Van der Laan, E., Gaboardi, S., Hilgen, F.J., Lourens, L.J., 2005. Regional climate and glacial control on high-resolution oxygen isotope records from Ain El Beida (latest Miocene, NW Morocco): a cyclostratigraphic analysis in the depth and time domain. Paleoceanography 20, PA1001.
Vasiliev, I., Reichart, G.J., Krijgsman, W., 2013. Impact of the Messinian Salinity Crisis on Black Sea hydrology—insights from hydrogen isotopes analysis on biomarkers. Earth Planet. Sci. Lett. 362, 272–282.
Vasiliev, I., Reichart, G.J., Krijgsman, W., Mulch, A., 2019. Black Sea rivers capture drastic change in catchment-wide mean annual temperature and soil pH during the Miocene-to-Pliocene transition. Glob. Planet. Chang. 172, 428–439. https://doi.org/10.1016/j.gloplacha.2018.10.016.
Violanti, D., Lozar, F., Dela Pierre, F., Natalicchio, M., Bernardi, E., Clari, P., Cavagna, S., 2013. Stress-tolerant microfossils of a Messinian succession from the Northern Mediterranean basin (Pollenzo section, Piedmont, northwestern Italy). Boll. Soc. Paleont. It. 52, 45–54.
Wei, W., Wise, S.W., 1992. Oligocene–Pleistocene calcareous nannofossils from Southern Ocean Sites 747, 748, and 751. In: Wise Jr., S.W., Schlich, R., et al. (Eds.), Proc. Ocean Drill. Prog., Sci. Results, 120, pp. 523–537. College Station, TX (Ocean Drilling Program).
Zachariasse, W.J., Lourens, L.J., 2021. The Messinian on Gavdos (Greece) and the status of currently used ages for the onset of the MSC and gypsum precipitation. Newsl. Stratigr. https://doi.org/10.1127/nos/2021/0677.